

Muscle activity analysis for passenger while riding moving train in prolonged standing: A case study

Fatimah Abdullah¹, Wan Hasrulnizam Wan Mahmood^{2,*}, Seri Rahayu Kamat¹, Siti Fatimah Afandi², M. Nur Othman²

¹) Faculty of Manufacturing Engineering, Universiti Teknikal Malaysia Melaka, Hang Tuah Jaya, 76100 Durian Tunggal, Melaka, Malaysia.

²) Faculty of Engineering Technology, Universiti Teknikal Malaysia Melaka, Hang Tuah Jaya, 76100 Durian Tunggal, Melaka, Malaysia.

*Corresponding e-mail: hasrulnizam@utem.edu.my

Keywords: Ergonomic; prolonged standing; muscle activity; KTMB Komuter

ABSTRACT – The purpose of this project is to analyze muscle activity between normal and obese women during train riding in prolonged standing position. A Surface Electromyography was used to measure passenger's muscle activity in the left and right of erector spinae, gastrocnemius and tibialis anterior. The muscle activity of the subjects was measured for 1 hours and 30 minutes of continuous prolonged standing during the beginning, middle and end of travel inside KTM Komuter Berhad from Pulau Sebang to KL Sentral station. The study concluded that prolonged standing give a muscle fatigue experienced to the passenger especially for those having obese BMI.

1. INTRODUCTION

There are various activities that can be done by using the muscle that is in our body. This activity of depends on the ability of muscles to perform the job within a certain period of time. While on board the train, there are various muscles in the human body that are used throughout the passenger's journey either standing or sitting position. These stand and sit position effects the level of muscle fatigue experienced by the user on board the train. People with prolonged stand condition are easy to get faster of muscle fatigue compared to those who get a seat. This muscle fatigue occurs when muscles are used above normal forces to achieve the desired level of strength. There are a lot of public user use train as their main transport to avoid a traffic jam. This causes the crowd of a passenger inside the train and contributes to the prolonged stand condition to the customer. A prolonged stand will contribute to discomfort and pain including lower back pain and musculoskeletal disorder [1] problem to the passenger.

In this study, we have investigated the muscle activity of female passengers with a normal BMI and those with high BMI (body mass index) values. They have to prolonged stand along the KTM Komuter train journey from Pulau Sebang/Tampin to KL Sentral which takes two hours. In particular, this study addresses three objectives. First is to examine the three muscles left and right of tibialis, erector spinae and gastrocnemius of a different type of women BMI when they have to prolonged stand for two hours journey inside a train. Second is to take a measurement of the involved muscle. And the last one is to evaluate which muscle has a high value in categories of train journey (begin, middle and end) between normal and obese BMI for

women passenger. It is hoped that this study will give awareness of which muscles will give a high value that contributes to the fatigue of the passengers who ride a train in prolonged standing.

2. METHODOLOGY

There were 23 subjects involved in this experiment with age ranging from 18 to 37 years old with no history of injuries for the past 12 months. The subjects have to prolonged stand with carrying 5 kg load behind them for one and a half hour in Women-Only Coach travel from Pulau Sebang/Tampin to KL Sentral. However, three females result in muscle activity was eliminated because they could not complete all experimental sessions. Among them, ten passengers were recruited from the normal BMI, and another ten were recruiting from obese BMI. Demographic of the selected passengers are described in Table 1.

Table 1 Demographic of the passengers (mean value).

Criteria	B.M.I	
	Normal	Obese
Age	22.9	22
Body Mass (kg)	59.5	91.2
Height (m)	1.59	1.59
Body Mass Index (BMI)	23.52	35.75

A surface Electromyography (TRIGNO TM Wireless System, TRIGNO TM Personal Monitor) and SJ4000 Action Camera were utilized to record, store and examine all the data regarding muscle activity of the 20 subjects. SEMG is one of the scientific instruments that have been applied to quantify muscle activity of passengers while riding moving train in prolonged standing. It quantifies the effort level of muscle in terms of myoelectric levels, expressed in Hertz (Hz) corresponding to contraction of the muscle while prolonged standing in a moving train. For instance, if myoelectric levels are high, it means that the muscles are exerting high effort while performing the particular tasks. This project uses the Trigno Wireless EMG system because it is quick and ease-of-use to apply the sensor in the muscle activity without medical supervision. The measurements of muscle activity were conducted based on the real-time monitoring. All electrodes were connected to a data logger and the

electromyography levels from the data logger are monitored through laptop screen using wireless networking. The sEMG electrodes were attached conscientiously to the subject's skin at the six left and right muscle; erector spinae, tibialis anterior and gastrocnemius as shown in Figure 1. The settings of sEMG follow the Non-Invasive Assessment of Muscles (SENIAM) procedure. The sEMG measurements were conducted for every 15 minutes of standing at the beginning (Pulau Sebang/Tampin station), middle (Seremban station) and end (Bandar Tasik Selatan station) of the journey travel. 15 minutes of the break was provided for every session, but respondents are not allowed to sit before completed all experiment sessions.

The raw signals from the sEMG measurement are interpreted through EMGWorks Analysis using software available in the sEMG system to determine muscle fatigue and video from the recorded camera have been rewind to analyzed subject's activity while they perform prolonged standing in a moving train. Statistical analysis was performed to examine the matrix relationship between the different type of BMI for begin, middle and end of traveling time with the different muscle as mention in Figure 1.

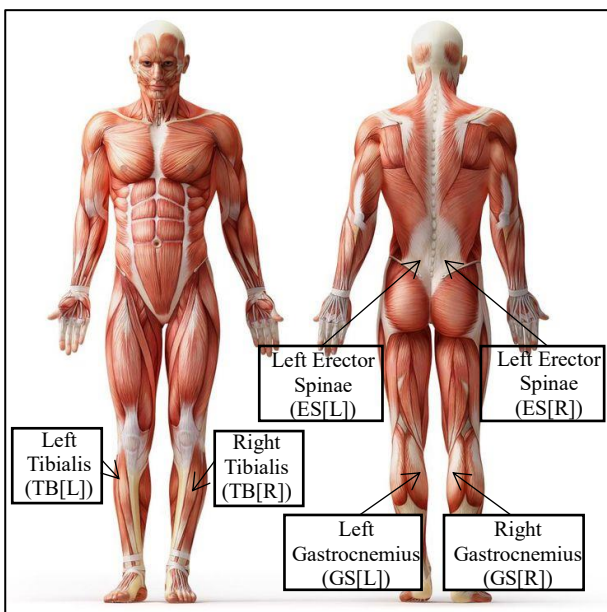


Figure 1 Muscle involve for sEMG measurement.

3. RESULTS AND DISCUSSION

Figure 2 result of sEMG measurement between normal and obese BMI using radar chart. The two types of BMI (normal and obese) are ranked on each of the six parameters (left and right of GS, TB, and ES) and divided into three scales of time (begin, middle and end). From the clear display data from the spider chart, the muscle value of the obese women gives a greater readability than the normal BMI woman who has a smaller scale. This means that obese women have higher muscle values than normal women of BMI. Other than BMI factor, BMI also affects the value of muscle activity for a person [2]. While the measurement of sEMG in the legs is felt maximum by the obese women at the gastrocnemius (left) at the beginning of the train

journey for the value of 214.2 Hz. This is because the muscle at this leg have to exert high effort to hold weight from an obese person at the beginning of the journey before it is get used to the prolonged standing condition. The minimum value also owned by an obese person in erector spinae (right) in the value of 179.7 Hz at the end of the journey. Looking at this result, it shows that obese subjects have a minimum value of muscle activity on the back of the body even though they have been standing for two hours along the train journey.

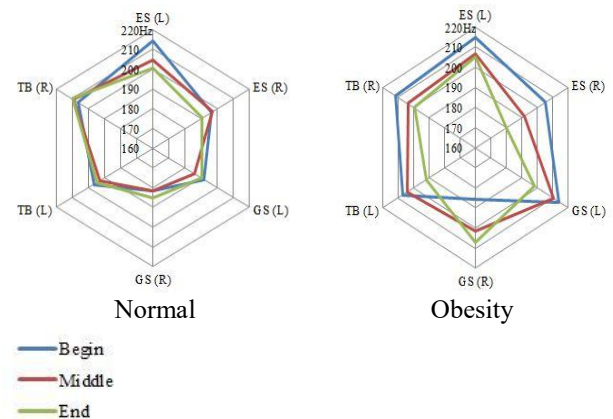


Figure 2 sEMG measurement for normal BMI and obese BMI.

4. CONCLUSIONS

This study concludes all passengers experienced fatigue in the lower back (ES), posterior legs (GS) and anterior legs (TB) when they have to prolonged stand inside train KTM Komuter Berhad. Through sEMG measurement, obese women have a maximum value than the normal person at the end of the train journey. It is hoped that the results of this study will users an awareness of the value of muscle they use if they have to prolonged stand for two hours. This project suggests anti-fatigue mat is positioned on the floor surface of the train to make passenger more comfortable along their journey.

ACKNOWLEDGEMENT

This research was co-funded by Universiti Teknikal Malaysia Melaka under research grant No. PJP/2016/PROTON/FTK-CARE/S01508, Ministry of Higher Education for MyBrain 15 Programme, KTM Komuter Berhad and Majlis Amanah Rakyat (MARA).

REFERENCES

- [1] Kamat, S. R., Halwanie, N., Fukumi, M., & Ito, T. (2017). Design a manual calf massager for prolonged standing workers by using ergonomic approach," in *The Japan Society of Mechanical Engineers International Conference*, 1–10.
- [2] Tomlinson, D. J., Erskine, R. M., Morse, C. I., Winwood, K., & Onambélé-Pearson, G. (2016). The impact of obesity on skeletal muscle strength and structure through adolescence to old age. *Biogerontology*, 17(3), 467–483.

Optimization of HHO generator zero current leak cell (ZCLC) model characteristics for improve gas productivity

Ajat Sudrajat^{1,2}, Noreffendy Tamaldin^{2,3,*}, Ahmad Kamal^{2,3}, Mohd Fadzli Bin Abdollah^{2,3}

¹⁾ Faculty of Science and Technology, Universitas Nasional-Jakarta,
JL. Sawo Manila, Pasar Minggu, Jakarta 12520, Indonesia.

²⁾ Faculty of Mechanical Engineering, Universiti Teknikal Malaysia Melaka,
Hang Tuah Jaya, 76100 Durian Tunggal, Melaka, Malaysia.

³⁾ Centre for Advanced Research on Energy, Universiti Teknikal Malaysia Melaka,
Hang Tuah Jaya, 76100 Durian Tunggal, Melaka, Malaysia.

*Corresponding e-mail: noreffendy@utem.edu.my

Keywords: HHO gas characteristic; HHO Generator; ZCLC model.

ABSTRACT- This paper investigates the current leaked on HHO generator which cause temperature rise resulted in HHO generator become hot, consequently HHO gas production quality decreased. One of the causes of electrical leakage is the erosion of holes in the cell plate electrodes. To overcome the problem, SS316L plate cell used as an electrode without the perforation, intended to suppress the rise in temperature caused by leakage current. This method is called zero current leak cell (ZCLC). Using the ZCLC method the HHO generator can produce optimal HHO gas [1], so gas production (liters per minute) is relatively stable compared to dry cells on hollow plate and has a composition of 67.6% of H₂ gas and 32.4% O₂. Test results on the dynamometer showed a positive effect on performance and engine emissions [5], with engine speed 1737rpm at 8A constant current produce the gas flow rate HHO 3.2lpm and can reduce gas CO and CO₂ up to 130ppm and 5.5%.

1. INTRODUCTION

With the increasing development of transportation technology and depleting of fossil fuel, hence the need for fuel, either in the form of oil or gas becomes a necessity that must be met by the government in the framework of energy stability. New Energy and Renewable Energy continue to be pursued by the Government in order to address the above needs by socializing the use of energy-saving and environmentally friendly technology.

Hydrogen is one of the energy that pertained to a new energy transportation fuel as a candidate of the most promising future. Various research on fuel cell vehicles sourced from hydrogen by the world's leading automotive industry since more than 50 years ago began to show a bright spot in the utilization of hydrogen-based fuel cell as a vehicle fuel. If the results of this study provide positive expected outcomes by the end of this decade will be an era of fuel cell cars throughout the world. At that point there will be a surge in demand of huge quantities of hydrogen [1].

This study discusses the hydrogen production process by using water as a medium in the process of electrolysis. The purpose of this study is to obtain optimal results as the fuel economy of the engine both

for a motor vehicle, generator sets as well as for another industrial engine. The new Energy from gaseous hydrogen is providing opportunities for development in developing countries for energy economist and environmentally friendly [4].

HHO generator developed at this time is still in development stage and have many weaknesses in particular to the influence of heat generated from the HHO generator. It is disrupting the volume and quality of HHO gas production. Therefore, it will greatly affect the performance of the engine. The heat generated from the HHO generator due to the leakage current that occurs through the holes in the stainless-steel plate cells move from one room to another. Studies have been conducted to resolve the leakage electric current with zero current leak cell (ZCLC) method [1].

Aim of this research to determine the actual change in engine performance that can be credited to the use of the HHO generator. The objectives of this research to measure the performance of a stationary engine (attached to a dynamometer) at a variety of engine loadings under its normal fueling arrangement, to repeat the same performance measurements when the HHO gas mixture from the HHO generator is used to supplement the fuel/air mixture, to measure the associated engine operating parameters affected by the combustion process, i.e. CO and CO₂ emissions, exhaust gas temperature, torque, rotational speed and to measure the HHO generator performance parameters, i.e. gas flow rate and current draw.

2. METHODOLOGY

Following pre-start checks the engine is started and run for 20 minutes under partial load to achieve normal operating temperatures through the system. The HHO generator is powered up and run for 20 minutes to ensure consistent temperature through the HHO generator body and to check the consistency of gas flow. Instruments are checked for consistency of readings until all are at a steady state.

The engine is run at 90% throttle for a range of torque loadings, i.e. 0 Nm, 20 Nm, 40 Nm, 60 Nm, 80 Nm and 100 Nm, and the engine speed is allowed to fluctuate. For each torque loading the engine is run for

10 minutes, first on diesel fuel alone and then supplemented with the gas mixture from the HHO generator at 3L/min. After 3 minutes settling time, instrument readings are taken every minute and then averaged and recorded. The engine test rig records total revolutions and the time so that an actual RPM can be calculated over a given period [3,5].



Figure 2: Test rig control panel



Figure 4: hho generator, power supply and supplementary measurement equipment



Figure 3: Potter diesel engine



Figure 5: test rig dynamometer

Figure 1 Testing equipment and set up.

The stationary engine is a Potter 2-cylinder diesel engine rated at 18kW at 1800 rpm, driving a dynamometer which can be loaded to a maximum of 100Nm. The engine-dynamometer rig incorporates control systems for managing and recording engine speed and torque. The exhaust gas emissions are sampled using a Kane 250 analyzer and the HHO generator flow rate is measured with a BOC oxygen specification gas flow meter. The power supply for the HHO generator is drawn from a 14V 10A DC lab rectifier and other measurements are taken using standard hand-held digital meters [5].

3. RESULTS AND DISCUSSION

3.1 Results

The results are recorded in Table 1 and graphs of important comparisons are given subsequently.

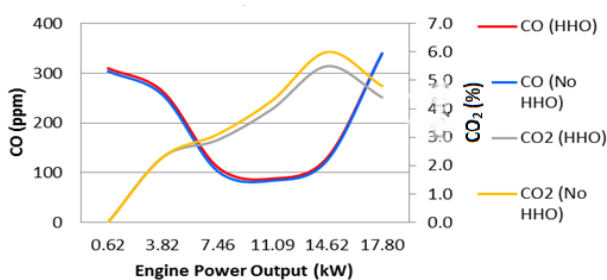


Figure 2 Changes in emissions due to HHO Generator use.

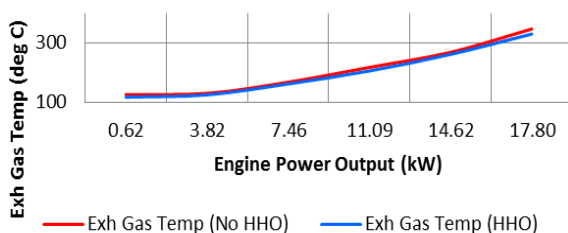


Figure 3 Changes in exhaust gas temperature due to HHO generator use.

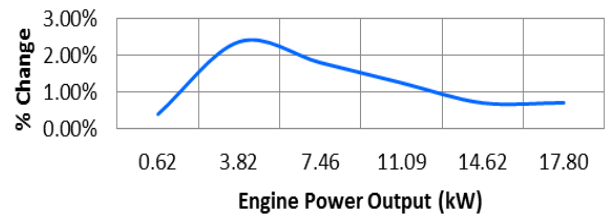


Figure 4 The percentage change in power output due to HHO Generator use.

3.2 Discussion

HHO gas generated by the HHO generator is very useful for improving the performance of the engine. The impact of HHO gas on the engine are consistently far greater in both gasoline and diesel engines. In testing an HHO generator to gasoline and diesel engines shows reduction in exhaust emissions of CO and CO₂ emissions as shown in Figure 2. The low exhaust gas temperature as shown in Figure 3 indicates a more efficient combustion process. The percentage of changes across various engine output (kW) with the use of HHO cell is shown in Figure 4.

The fuel consumption can be measured directly, but a mechanism for the flow of fuel to the injectors may not be changed substantially and the machine will only receive a supply of any fuel available, including additional HHO gas. By using HHO gas, there will be also efficient use of fuel in the engine [4].

4. CONCLUSIONS

In conclusion, it was observed that the use of HHO generator in internal combustion engine have positively affected the engine performance. It also has a measureable effect on the engine operating parameters. The effects are beneficial in term of engine performance and exhaust emissions.

Further work needed to evaluate the HHO generator on a more sophisticated test rigs which allow more extensive parameters to be measured. Further study would also focus on new generation of HHO generator to overcome some of the issues addressed in this study.

ACKNOWLEDGEMENT

This project is an extended work previously supported by Ministry of Education Malaysia under the grant FRGS/2012/FKM/TK08/02/1/F 00140. This work is also partly supported by UTeM internal grant PJP/2017/FKM-CARE/S01564.

The authors would like to acknowledge the members from Green Tribology and Engine Performance (G-TriboE) Research Group, Centre for Advanced Research on Energy (CARE), Faculty of Mechanical Engineering, Universiti Teknikal Malaysia Melaka and Fakultas Teknik & Sains, Universitas Nasional, Jakarta, Indonesia UNAS for continuous support in this study.

REFERENCES

- [1] Reddy, D., & Krishnamurthy, B. (2018). Analyzing leakage current in a direct methanol fuel cell. *Journal of Solid State Electrochemistry*, 1-14.
- [2] bin Rosley, M. N., bin Tamaldin, N., Abdollah, M. F. B., & Zulfattah, Z. M. (2015). The Effects of Voltage Flow and pH Value in Alkaline Electrolyser System to Performance. *Applied Mechanics and Materials*, 773, 440-444.
- [3] Rosley, M. N., Tamaldin, N., Abdollah, M. F., Zakaria, M. Z., Yamin, M., & Kamal, A. (2006). Emission characteristics of hydrogen enrichment in light duty single cylinder diesel engine. *ARPJ Journal of Engineering and Applied Sciences*, 12, 4255-4258.
- [4] Sonthalia, V., Mallya, M. R., Sonthalia, A., & Sridhar, K. S. (2014). Experimental analysis of hydro enhanced automobile engine. *International Journal of Emerging Technology and Advanced Engineering*, 4(8), 445-453.
- [5] Carmo, M., Fritz, D. L., Mergel, J., & Stolten, D. (2013). A comprehensive review on PEM water electrolysis. *International journal of hydrogen energy*, 38(12), 4901-4934.
- [6] Hussain, G., Sofianos, M. V., Lee, J., Gibson, C., Buckley, C. E., & Silvester, D. S. (2018). Macroporous platinum electrodes for hydrogen oxidation in ionic liquids. *Electrochemistry Communications*, 86, 43-47.
- [7] Göllei, A. (2014). Measuring and optimisation of HHO dry cell for energy efficiency. *Acta Technica Corviniensis-Bulletin of Engineering*, 7(4), 19-22.
- [8] EL-Kassaby, M. M., Eldrainy, Y. A., Khidr, M. E., & Khidr, K. I. (2016). Effect of hydroxy (HHO) gas addition on gasoline engine performance and emissions. *Alexandria Engineering Journal*, 55(1), 243-251.
- [9] Uludamar, E. (2018). Effect of hydroxy and hydrogen gas addition on diesel engine fuelled with microalgae biodiesel. *International Journal of Hydrogen Energy*. In press.
<https://doi.org/10.1016/j.ijhydene.2018.01.075>

Table 1 Test results

Start Time	Lapsed time (s)	Engine speed (rpm)	Total revs	Calculated rpm	Rads/s	Torque (Nm)	Power (W)	% Change in power	Dyno Load (A)	HHO flow (LPM)	HHO Load(A)	CO ppm	CO ₂ %	Exh T (°C)
10.24	600	1863	18631	1863.1	195.1	3.2	0.62		0	0.0	0.0	304	0.0	125
10.45	600	1870	18704	1870.4	195.9	3.2	0.63	0.39%	0	3.0	7.9	310	0.0	116
10.57	606	1814	18330	1814.9	190.1	20.1	3.82		10	0.0	0.0	256	2.3	129
11.05	600	1814	18128	1812.8	189.8	20.6	3.91	2.37%	10	2.9	8.1	263	2.3	124
11.24	555	1772	16431	1776.3	186.0	40.1	7.46		21	0.0	0.0	103	3.1	167
12.11	540	1783	16035	1781.7	186.6	40.7	7.59	1.80%	21	3.0	8.0	111	2.9	161
12.27	480	1751	14096	1762.0	184.5	60.1	11.09		35	0.0	0.0	84	4.3	217
12.38	420	1754	12324	1760.6	184.4	60.9	11.23	1.25%	35	3.1	8.1	88	4.0	205
12.51	300	1738	8717	1743.4	182.6	80.1	14.62		46	0.0	0.0	125	6.0	268
13.03	353	1737	10252	1742.5	182.5	80.7	14.73	0.70%	46	3.2	8.1	130	5.5	261
13.16	309	1715	8897	1727.6	180.9	98.4	17.80		60	0.0	0.0	340	4.8	347
13.31	163	1720	4712	1734.5	181.6	98.7	17.93	0.71%	60	3.1	8.1	340	4.4	330

Parametric study on braking dynamics of motorcycle

Arif Pahmi^{1,2,*}, M. Hisyam Basri^{1,2}, R.J. Talib^{1,2}, Amiruddin Mohd Ayob¹, Hazim Sharudin¹

¹⁾ Faculty of Mechanical Engineering, University of Technology MARA,
Pulau Pinang, 13500 Permatang Pauh, Pulau Pinang, Malaysia.

²⁾ Automotive Research and Testing Center (ARTeC), University of Technology MARA,
Pulau Pinang, 13500 Permatang Pauh, Pulau Pinang, Malaysia.

*Corresponding e-mail: arif.hamid.pahmi@ppinang.uitm.edu.my

Keywords: Rider weight; pillion weight; deceleration

ABSTRACT – Motorcycle brake system is used to decelerate and maintaining speed. This study is to investigate rider weight, pillion weight and brake pads effect on the braking dynamics performances. The test is conducted in accordance to ECE R78 where the speed is maintained at 60km/h before the motorcycle is brought to totally stop. The results showed rider weight at 65kg has the highest deceleration using different brake shoes. Pillion weight exhibits significant effect to the deceleration. It can be concluded that rider weight, pillion weight and brake shoe are important factors in the motorcycle braking.

1. INTRODUCTION

In general, the main functions of the braking system for motorcycles are to maintain the vehicles speed while driving downhill, to decelerate the motorcycle and to fully stop the motorcycle. During braking action, pulling the brake cable or pushing the brake pedal created forces that are transmitted to the brake shoes and reducing the rotation of the brake drum.

Stopping mechanisms in the motorcycle are the part that controls vehicle within the desired speeds. The vehicle should be able to start moving it, make some turn, accelerate, decelerate and most important is to stop it [1]. In the drum brake system, the force exerted between the linings and the drum depends upon the coefficient of friction of the two materials, form applied between the skiing surface, the roughness of the surface, and the material of which the surface is made. The performances of braking system are not only assessed based on a stop but other factors such efficient in all speeds, wind and temperatures [2]. In addition, motorcycle brake systems also need to be maintained properly so that the system is in good condition.

Most experts agree that roughly 70% of braking effort should go to the front wheel (which uses the hand lever on the right grip), and 30% to the rear (which is operated by the right foot pedal.) When there is less down force on the rear tire, it becomes much easier to lock up and slide that wheel, resulting in a loss of control [3]. Although the braking torque at the rear wheel is rather small compared to the front-wheel one, on a strong braking maneuver the effect of the rear brake can be clearly appreciated [2]. Normal stops should still be made by using both the front and rear brake. The rear brake can

still be quite powerful and on a cruiser, where more of the weight is positioned over the rear, it is more important.

In this study, effect of rider weight, pillion weight and brake pads on the motorcycle braking is investigated. A set of rider weights and pillion weights apparently has an effect on weight distribution of motorcycle during braking. Additionally, brake pads from different manufacturers would expect to influence braking performances. This study limited to drum brake system and small engine capacity motorcycle. (below 150cc)

2. METHODOLOGY

The testing is conducted in accordance to Economic Commission for Europe Regulation 78 (ECE R78). The selected road has a flat surface, dry condition and is a straight road. The speed of motorcycle has been set to 60km/hr for every braking testing. The speed limit is to ensure that motorcycle safety on the road during research carried out. The experiment used Modenas motorcycle Kriss 100 cc. Road length between 150-200 meter is used to reach the speed limit 60km/hr before applying both front and rear brake system. The brake was gradually applied until maximum applied force after the motorcycle reaches speed 60km/h to bring the motorcycle totally stop. Table 1 listed motorcycle specification used in the on-road testing.

Table 1 Motorcycle specification.

Item	Specification
Engine type	Single cylinder, four-stroke
Fuel system	Carburetor, Keihin PB18X1
Transmission	4-speed
Lubrication system	Force lubricating wet
Brake system	Front: Drum Rear: Drum

Three levels full factorial method is employed to organize the on road testing. Three variables chosen for the study were pillion weight, rider weight and types of brake shoes with range 65kg to 85kg. The types of brake shoes are designated as A, B and C as shown in table 2. During the testing, the speed of motorcycle was kept constant at 60km/h based on ECE R78.

3. RESULTS AND DISCUSSION

3.1 Effect of rider weight and brake shoes on deceleration

The effect of different of rider weight and brake shoes on deceleration at speed of 60km/h is shown in Figure 1. The results showed that the lowest rider weight will benefit to improve deceleration during braking. It was observed that the rider weight of 65kg recorded the highest deceleration when applying both of brake system. The decelerations of 65kg of rider weight showed highest when using brake shoe A and C, whereas brake B indicated the lowest deceleration. Similar trends of deceleration were found for rider weight of 75kg and 85kg whereas the peaks at 3.0m/s^2 and 2.7m/s^2 when using brake shoe B. The highest of deceleration of brake A and C for the rider weight 65kg are influenced by selecting the good quality of brake shoes. It was proved by the graph that the trend of 65kg when using brake A and C get highest deceleration on the braking test. Therefore, selecting the type of brake shoes and rider weight are significant factors to maximize the deceleration of the motorcycle when applying both of braking system.

Table 2 Factors and levels.

Factor	Level		
	1	2	3
Rider (kg)	65	75	85
Pillion (kg)	65	75	85
Types of brake shoe	A	B	C

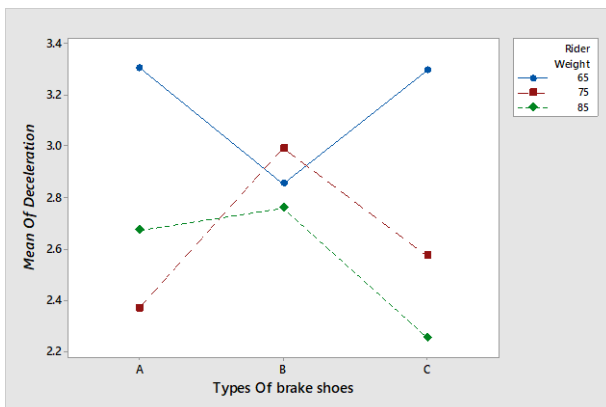


Figure 1 Effect of rider weight and types of brake shoes on deceleration.

3.2 Effect of rider weight and pillion weight on deceleration

Effect of rider weight and pillion weight on deceleration can be seen at Figure 2. The highest of deceleration is for rider that have weight 65 kg. It shows that, for the pillion weight of 65kg, 75kg and 85kg the deceleration indicated highest peak about 3.35m/s^2 , 3.3m/s^2 and 2.9m/s^2 for rider weight 65kg. In comparison, adding pillion on the motorcycle will increase the performance of deceleration. In addition, the deceleration showed decrement due to the increase of the

weight of pillion. However, for rider that weight 75kg showed constantly of the deceleration for weight of pillion weight 75kg and 85kg. In addition, for rider weight 85 kg has less deceleration for all weight of pillion. It can be concluded that the weight of rider and the weight of pillion will affect deceleration. As a result, the high of weight of rider and pillion give impact for the low deceleration.

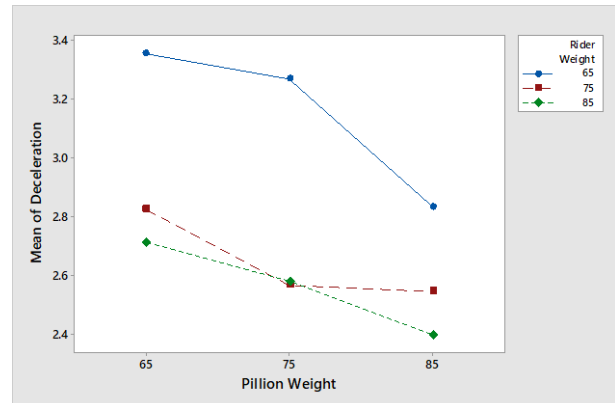


Figure 2 Effect of rider weight and pillion weight on deceleration.

4. CONCLUSION

The effect of rider weight, pillion weight and brake shoes were completed in the testing to investigate the deceleration braking performance. The rider weight 65kg exhibits the highest point for both variations of brake shoes and pillion weight at deceleration 3.3m/s^2 . The trends of deceleration are inconsistent because of the rider behaviors during applying braking. Some of the riders tend to press the brake lever very fast and as a result the quick braking response. In addition, braking deceleration reduced upon consideration pillion weight effect in the testing. Based on study, there is no simple correlation between rider weight, pillion weight and brake shoe. In future, the testing requires rider to apply consistence braking to get consistent decelerations.

ACKNOWLEDGEMENT

This research was supported by the Ministry of Sciences, Technology and Innovation, Malaysia (MOSTI), with science fund grant No. 06-01-01-SF0809. The authors would like to thank Universiti Teknologi MARA for providing the research facilities.

REFERENCES

- [1] Day, A. J. (2014). *Braking of road vehicles*. Butterworth-Heinemann.
- [2] Corno, M., Savaresi, S. M., Tanelli, M., & Fabbri, L. (2008). On optimal motorcycle braking. *Control Engineering Practice*, 16(6), 644-657.
- [3] Belmonte, J., Bouchard, J. P., Gregoire, S., Robitaille, Y., & Cooper, P. (2003). Performance evaluation for various braking systems of street motorcycles. *Promocycle Found.*

Slider crank mechanism system for flapping wing MAV's: Kinematic analysis

Hamid Yusoff, Koay Mei Hyie, Salina Budin, Dzullijah Ibrahim, Rosniza Rabilah, Shafiq Suhaimi*

Faculty of Mechanical Engineering, Universiti Teknologi MARA, Cawangan Pulau Pinang, Kampung Tok Ebot, 13500 Permatang Pauh, Pulau Pinang, Malaysia.

*Corresponding e-mail: shafiq.suhaimi@gmail.com

Keywords: Flapping wing; micro air vehicles; low aspect ratio

ABSTRACT – This paper focuses on the design of an electro-mechanical device for studying the inertial effect of flapping wings. The device is designed to mimic the flight behavior of bat wing flight. The design device consists with three main systems namely, mechanical, electrical and force measurement system. Wing flapping amplitude could be varied from 40° , 50° to 60° during down and up stroke by changing the rotating arm length according to the bat flight model investigation from previous literature [5]. The kinematic mechanisms of flapping model were analyzed using analytical model where the angular displacement, angular acceleration, angular velocity, and tangential acceleration over the crank angle was calculated.

1. INTRODUCTION

Micro Air Vehicle (MAV) is defined as a small, portable flying vehicle which is designed for flying in small and tight areas. There are three generations of MAVs namely fixed wings, rotating wings (like helicopters) and wing based on micro-technologies (MEMs, flapping or vibrating wings) [1]. Flapping wings can potentially provide much greater aerodynamic efficiencies than propellers and rotors of comparable size for low Reynolds number flight [1-3]. They could penetrate the rubble regardless of any "terrain" obstacles that could stop other vehicles. Ability to fly forward and hover efficiently and maneuver in confined spaces. On the other hand, high airspeed is not necessary and may be disadvantageous in some cases. The focus in this paper is the development and design of an electro-mechanism system to realize the flapping motion for a bat-inspired flapping wing.

2. LITERATURE REVIEW

A bat's wing is built on the basic pattern of a mammalian limb. It is an analogous structure to the human arm and hand (in fact, the name "chiroptera" is Greek for "handwing"). The bat also has unique muscles in the patagium, chest and back, to power the wing during flight. The wing consists of the arm, wrist and hand. The bones of the hand and the four fingers are greatly elongated, light and slender to provide support and manipulate the wing membrane, called the patagium [4].

The shape of the wing varies greatly from a species to another. Smaller wings reduce the weight of the animal and give it a greater endurance in flight.

However, wings should be large enough to carry the creature. Broad wings will slow its flight but will give the animal better maneuverability. Narrow wing will allow a faster but less control flight [5].



(a) Broad wings: Maneuverability
(b) Narrow wings: High speed

Figure 1: Wing shape of bat wing and skeleton structure orientation.

3. EXPERIMENTAL DEVICE DESIGN

In general, previous studies [4-5] have shown that the variation of Wing beat amplitude increase directly with increasing of the flight speed, and the wing beat frequency decrease slowly decrease with increasing of flight speed. The minimum and maximum values were between 4 to 13 Hz for wing beat frequency, and their Wing beat amplitude limits of approximately 40° to 100° measured for 23 species of Australian bat, representing two sub-orders and six families. To replicate this, a flapping mechanism was designed where, in the mechanism a crank and slider are connected by means of connecting rod. The slider is free to move in a vertical slot or guides and convert the 360-degree rotational motion to wing flapping motion with the amplitude adjustable for 40 to 60 degrees. The rockers which carries flapping wing are hinged at a suitable distance from the vertical sliding slider. This is mainly governed by the stroke of the slider and the flapping angle amplitude required. These rockers are slotted at the end and connected to the slider by means of circular rod which takes care of the variation in the distance and also permits the rockers to perform the flapping motion, as seen in Figure 2.

The kinematic analysis was done using a simulink model that was developed based on the governing equations. The lengths of the crank angle and connecting rod are resolved into vertical and horizontal components.

$$b \sin \theta_2 = a \sin \theta_3 \quad (1)$$

Displacement of the slider is given by

$$s = b \cos \theta_3 + a \cos \theta_2 \quad (2)$$

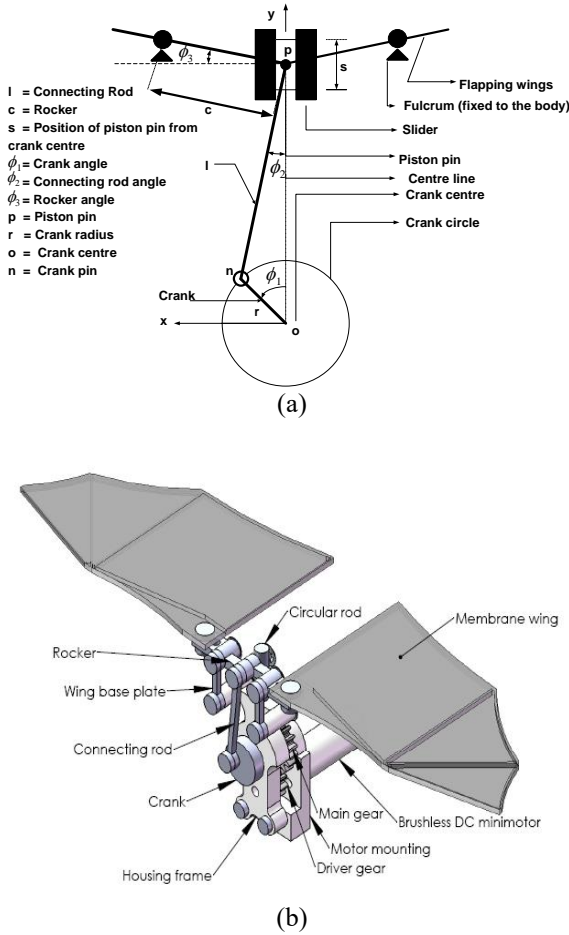


Figure 2: Mechanism design where: (a) is the schematic diagram and (b) is the CAD drawing.

The input θ_2 is given at the crank so the angle θ_2 can be obtained by solving the equation 2. Displacement of the slider can be obtained from equation 3. The angle rockers make with the horizontal can be calculated using the equation 3 given below.

$$\sin \theta = \frac{s-b}{c} \quad (3)$$

Angular velocity right crank angle takes first derivative, using the chain rule, can be simplified by through Equation 5;

$$\frac{d\theta}{dt} = \frac{1}{10 \cos \theta} \left[\frac{d\theta_2}{dt} \right] \left\{ -b \sin \left[\sin^{-1} \left(\frac{a \sin \theta_2}{b} \right) \right] \right\} \frac{1}{\sqrt{1 - \left(\frac{a \sin \theta_2}{b} \right)^2}} \frac{a}{b} \cos \theta_2 - a \sin \theta_2 \quad (4)$$

An acceleration write crank angle takes second derivative, using the chain rule and the quotient rule in Equation 6:

$$\frac{d^2\theta}{dt^2} = \frac{1}{10 \cos^2 \theta} \left[\frac{d^2\theta_2}{dt^2} \right] \left\{ \begin{aligned} & \left[\sin \left(\sin^{-1} \left(\frac{a \sin \theta_2}{b} \right) \right) + \theta \right] \\ & + \sin \left(\sin^{-1} \left(\frac{a \sin \theta_2}{b} \right) \right) - \theta \end{aligned} \right\} \frac{1}{\sqrt{1 - \left(\frac{a \sin \theta_2}{b} \right)^2}} \frac{a}{b} \cos \theta_2 + 1 \quad (6)$$

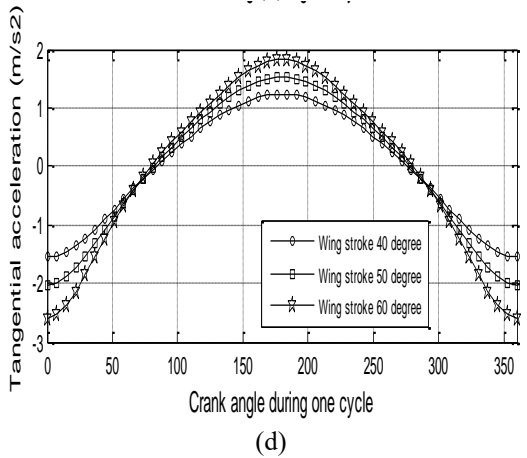
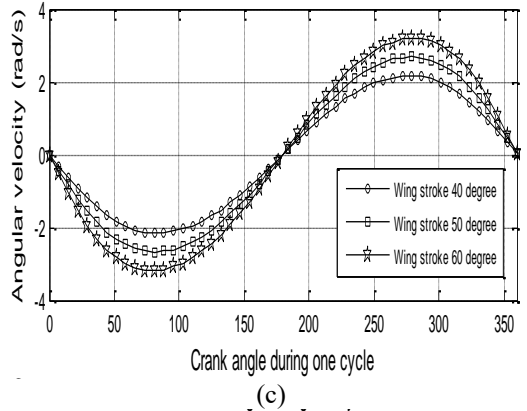
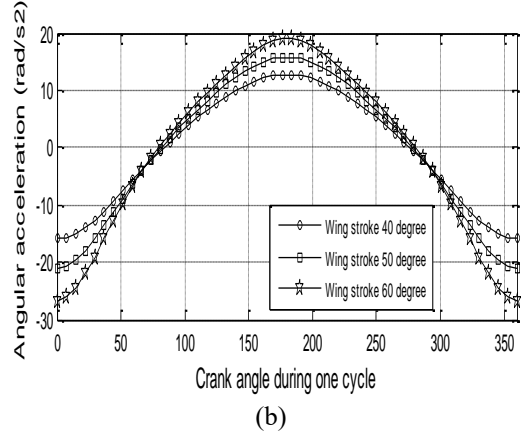
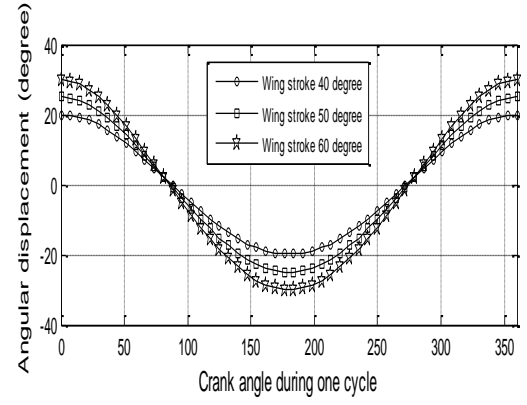


Figure 3: Kinematics analysis for one cycle where: (a) is the angular displacement against crank angle (b) angular acceleration over crank angle (c) Angular velocity over crank angle (d).

4. CONCLUSIONS

The main objective of this study is to design a crank system of a flapping wing based inspired by bats. A Simulink model was developed and the angular displacement, angular acceleration, angular velocity, and tangential acceleration over crank angle was calculated. The resulting data can later be used for aerodynamic study of the wing design as well as calculating the inertial and power requirements of the mechanism itself.

REFERENCES

- [1] Lin, C. S., Hwu, C., & Young, W. B. (2006). The thrust and lift of an ornithopter's membrane wings with simple flapping motion. *Aerospace Science and Technology*, 10(2), 111-119.
- [2] Sun, M. (2005). High-lift generation and power requirements of insect flight. *Fluid Dynamics Research*, 37(1-2), 21-39.
- [3] Hou, Y., & Kong, J. (2008, October). Bionic Flying Robot: Design, Fabrication and Experiment. In *International Conference on Intelligent Robotics and Applications* (pp. 188-196). Springer, Berlin, Heidelberg.
- [4] Aldridge, H. D. (1986). Kinematics and aerodynamics of the greater horseshoe bat, *Rhinolophus ferrumequinum*, in horizontal flight at various flight speeds. *Journal of Experimental Biology*, 126(1), 479-497.
- [5] Thollessen, M., & Norberg, U. M. (1991). Moments of inertia of bat wings and body. *Journal of Experimental Biology*, 158(1), 19-35.
- [6] Galiński, C., & Żbikowski, R. (2007). Some problems of micro air vehicles development. *Bulletin of the Polish Academy of Sciences. Technical Sciences*, 55(1), 91-98.
- [7] Swartz, S., Iriarte-Diaz, J., Riskin, D., Tian, X., Song, A., & Breuer, K. (2007). Wing structure and the aerodynamic basis of flight in bats. In *45th AIAA Aerospace Sciences Meeting and Exhibit* (p. 42).
- [8] Shyy, W., Berg, M., & Ljungqvist, D. (1999). Flapping and flexible wings for biological and micro air vehicles. *Progress in Aerospace Sciences*, 35(5), 455-505.

Design and fabrication of small subsonic wind tunnel

Hamid Yusoff, Ahmad Sufian Abdullah, Halim Ghafar, Aliff Farhan Mohd Yamin, Nor Suhada Abdullah, Siti Nur Amalina Mohd Halidi, Mohd Bahir Mohd Yusuf, Shafiq Suhaimi*

Faculty of Mechanical Engineering, Universiti Teknikal MARA, Cawangan Pulau Pinang, Kampung Tok Ebot, 13500 Permatang Pauh, Pulau Pinang, Malaysia.

*Corresponding e-mail: shafiq.suhaimi@gmail.com

Keywords: Sub-sonic flow; wind tunnel

ABSTRACT – The purpose of this study is to design and fabricate a small subsonic wind tunnel that can produce a free stream velocity of up to 14.5m/s. The size of the test section was 0.25m x 0.24m x 0.5m. A velocity profile test was done at different parts of the test section (at 14.5 cm, 25cm, and 35.5cm) which yields a small variation of wind speed between the different parts of the test section. This shows that the produced wind is reasonably uniform. The wind tunnel was made for aerodynamic performance testing of an object at a subsonic speed.

1. INTRODUCTION

A wind tunnel is a well-known that can be used to test the aerodynamic properties of a certain object at different wind speed settings [1]. A subsonic wind tunnel means that the wind speed used in the aerodynamic setting is less than Mach 1. A wind tunnel has a wide application in engineering ranging from aircraft design to automotive design to the design of a building. The main objective of this study is to design and fabricate a small subsonic wind tunnel that can produce a uniform airflow with a wind speed of up to 14.5m/s.

2. LITERATURE REVIEW

For the case of this study, the wind tunnel that is being designed is a small sub-sonic open circuit wind tunnel. As mentioned before, a sub-sonic wind tunnel means that the wind tunnel operates at wind speed lower than Mach 1 [2]. Open circuit indicates that the moving air comes from the surrounding from one end of the other end of the tunnel circuit.

The parts that needed to be considered in an open circuit wind tunnel are; the settling chamber, the contraction cone, the test section, the diffuser, and the honeycomb.

The settling chamber is the part of the wind tunnel that smooth the incoming air. Inside the settling chamber includes the honeycomb which eliminates the oncoming turbulence, and the contraction cone which matches the correctional area of the inlet to the test section [3]. The key factors that needed to be considered in designing a honeycomb is the length of the honeycomb itself, the cell hydraulic diameter, and the porosity. For the honeycomb to be effective, the porosity (which is defined as the ratio between the area of the air flow to

the total cross-sectional area) must be greater than 0.8, and the ratio between the length of the honeycomb to the hydraulic diameter is between 6 and 8 [4]. As for the contraction cone, the ratio between the inlet and the final correctional area must be around 6 to 10 [5].

The diffuser slows down the speed of the airflow at the outlet of the wind tunnel. This is important as to prevent any misfortunes that might occur during testing. A diffuser must have a ratio between the inlet and outlet cross-sectional area under 2.5 and have a diffuser point of between 5°-7° [6].

3. WIND TUNNEL DESIGN

The design of the wind tunnel itself was done using the Solidworks software. The overall design was based around the test section. The test section needed to have a cross-section area of 0.25m x 0.25m with a length of 0.5m, as shown in Figure 1. This is to accommodate the size of the tested object.

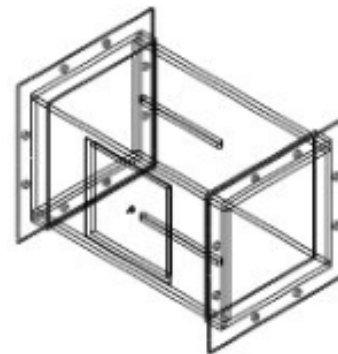


Figure 1 Test section design.

From the size of the test chamber in Figure 2, the contraction cone can be set to the size of the test section. Therefore, the outlet cross-section area of the contraction cone size will be the same as the test section area which is 0.25m x 0.25m. The inlet area of the contraction cone will be 0.75m by 0.75 to keep the ratio between the inlet and outlet between 6 to 10 (in this case, 9). The length of the contraction cone will be 1m.

From Figure 3, the size of the settling chamber is based on the size of the outlet cross sectional area of the contraction cone, which is 0.75m x 0.75m. The length was set as 0.375m as to fit the honeycomb.



Figure 2 Contraction design.



Figure 3 Settling chamber design.

The length of the honeycomb, as shown in Figure 4, was set at 7.5cm and the hydraulic diameter was set at 1.2cm. This is because the ratio between the length and hydraulic diameter of the honeycomb to be between 6 to 10 (in this case, 6.2).



Figure 4 Honeycomb design.

From Figure 5, the inlet area was set to the area of the test section (0.25m x 0.25m). The outlet area was set at 0.3m x 0.3m so that the ratio between the inlet and outlet area was set below 2.5 (in this case 0.6944). The length of the diffuser was set at 2m.

The design was then fabricated, as shown in Figure 6. The settling chamber and the contraction cone was made from sheet metal. The test section was made from transparent acrylic while the diffuser was made of wood.



Figure 5 Diffuser design.



Figure 6 The fabricated wind tunnel.

4. AIRFLOW TEST

Once the fabrication was done, the airflow was then tested to determine the quality of the airflow. The airflow was measured using Extech HD350 Digital Differential Manometer. The airflow was set at 14.5m/s. The was measured from the bottom wall to the top wall of the test section with a 2cm increment. The test was done at points of the test sectional; 14.5cm, 25cm, and 35.5cm from the inlet of the test section. The result is shown in Figure 7.

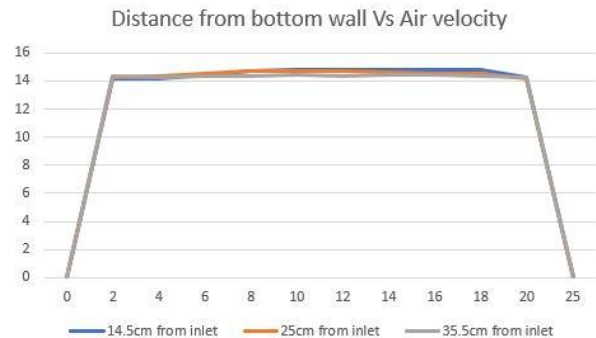


Figure 7 Air velocity profile at the test section.

From the result it has been shown that there are small variations between the points in the test chamber. This shown that there is no velocity difference along the length of the test chamber showing that the flow resulting airflow is reasonable uniform and has no vortices.

5. CONCLUSIONS

The airflow test has shown that there are small variations along the length of the test section. This have shown that the air is reasonably uniform. The designed wind tunnel will the be used to test the aerodynamic performance of an object in a future project.

REFERENCES

- [1] Onyenanu, I. U., Ezeonuegbu, I. H., & Mobi, I. M. Design and fabrication of a subsonic wind tunnel testing machine for use in Nigerian universities. *International Journal of Engineering and Technical Research*, 1(8), 84–90.
- [2] Barlow, J. B., Rae Jr, W. H., & Pope, A. (2015). Low speed wind tunnel testing. *INCAS Bulletin*, 7(1), 133.
- [3] Nordin, N., Karim, A., Ambri, Z., Othman, S., & Raghavan, V. R. (2013). Design and development of low subsonic wind tunnel for turning diffuser application. *Advanced Materials Research*, 614, 586-591.
- [4] Nathan T. (2008). Wind tunnel design and operation. *Thesis*.
- [5] Bell, J. H., & Mehta, R. D. (1988). Contraction design for small low-speed wind tunnels. *NASA STI/Recon Technical Report N*, 89.
- [6] Worthey. (2006). Subsonic wind tunnels. *Wind Tunn. Connect*.

Mathematical modeling of passive car suspension systems on sinusoidal road profile

Adam Samsudin^{1,*}, Shamsuddin Ahmad², Ezzatul Farhain Azmi¹

¹) Faculty of Engineering Technology, Universiti Teknikal Malaysia Melaka, Hang Tuah Jaya, 76100 Durian Tunggal, Melaka, Malaysia.

²) Faculty of Science, Universiti Teknologi Malaysia, 81310 Skudai, Johor, Malaysia.

*Corresponding e-mail: adam.samsudin@utem.edu.my

Keywords: Mathematical Modeling; car suspension; road profile

ABSTRACT – Suspension systems have been widely applied to vehicles. It gives a comfortable ride to the driver across many type of road profile. A simple mathematical model of a passive quarter car suspension system has been formulated analytical to determine whether the suspension of car model will give a comfortable ride. This study is using Ford Scorpio car model data that are being applied to sinusoidal road profile with considering the basic quarter car model and the refinement of the basic quarter car model.

1. INTRODUCTION

A suspension system has been applied to vehicles and plays a vital role to smooth out the ride while maintaining excellent control. A good suspension system should provide a comfortable ride and good handling within a reasonable range of deflection [1]. Basically, the function of a car suspension system is to keep the car's wheels in firm contact with the road [2]. This may sound simple, but with acceleration comes force, and forces convert into raw energy, when vehicle accelerates down a road bump will cause forward energy to be converted into vertical energy, which travels through the frame of the vehicle. Without coil and springs to absorb this, vertical energy would cause vehicles to jump up off the road, reduce tire friction and control. The car will then come bounding back down with even greater force, making for a very uncomfortable and dangerous ride. Therefore, the car suspension system needs to be investigated and suspension for car also has their potential to improve vehicle performance.

2. METHODOLOGY

In this study, we formulate a basic quarter car suspension model by a 'sinusoidal road profile'. Numerical solution of 4th order Runge-Kutta method is used in Maple 13 to solve the suspension system. Which, the result of a car suspension system for simple and refinement model can be shown graphically.

2.1 Model analysis

Figure 1 and Figure 2 shows the force diagram of simple and refined car model, where we are able to formulate a mathematical suspension system with satisfying Newton's second law of motion.

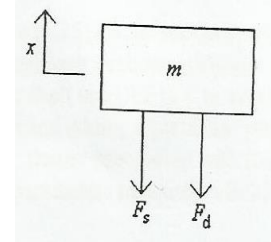


Figure 1 Force diagram of simple car.

By applying the Newton's second law of motion, the equations of the simple car motion can be found as in Equation (1).

$$m\ddot{x} + c\dot{x} + kx = ky + c\dot{y} \quad (1)$$

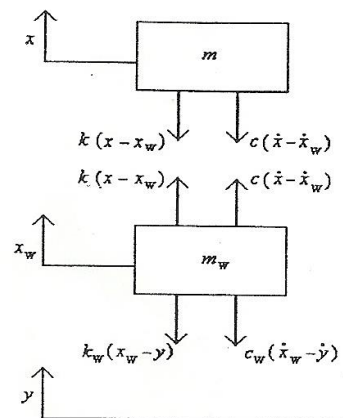


Figure 2 Force diagram of refinement car.

And, the equations of the refinement simple car motion can be converted into Equation (2) and Equation (3).

$$m\ddot{x} = -k(x - x_w) - c(\dot{x} - \dot{x}_w) \quad (2)$$

$$m_w\ddot{x}_w = k(x - x_w) - c(\dot{x} - \dot{x}_w) - k_w(x_w - y) - c_w(\dot{x}_w - \dot{y}) \quad (3)$$

Where, m is mass of the car, c is the constant representing the damping of the spring, k is the constant representing the stiffness of the spring, x is the vertical displacement of car body above its equilibrium position, y is the vertical displacement of the wheel due to the road surface, x_w is the difference between the car body, wheel and axle.

2.2 Sinusoidal road profile

Assume that the car is travelling with an average horizontal speed, V and hence that $z = Vt$. Where, z is horizontal displacement and t is time travel. By making this assumption, the form for y can be expressed as:

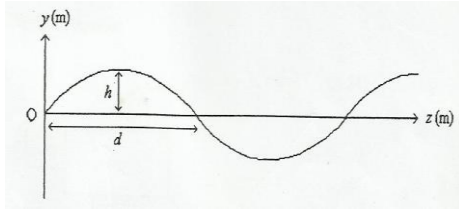


Figure 3 Sinusoidal road profile

$$y = h \sin\left(\frac{\pi Vt}{d}\right)$$

$$\dot{y} = h \left(\frac{\pi Vt}{d}\right) \cos\left(\frac{\pi Vt}{d}\right)$$

Where, h is height of the sinusoidal road profile and d is the distance.

3. RESULTS AND DISCUSSION

The good suspension system should satisfy the prediction by graph,

- I. $|x| \leq 0.1$ for all value of time, t .
- II. $|\ddot{x}| \leq 0.6g$ for all value of time, t .

Where, g is the gravitational force.

Figure 3 and Figure 5 indicate the vertical displacement of simple and refined car model. Meanwhile, Figure 4 and Figure 6 indicate a vertical acceleration of simple and refinement car model. Both plotting graphs of displacement for simple and refinement car model shows that it bound implied the prediction I.

However, the graph of acceleration for simple car unsatisfied the prediction in II, where the acceleration is found out greater than $0.6g$. From both graphs of refinement car model, it shows that the oscillation gives a smaller value compared to simple car model. Both graphs for refinement model also show changes approaching to zero when time goes by 100 second. Whereas, the displacement and acceleration involve from simple car model remain unchanged in 20 second.

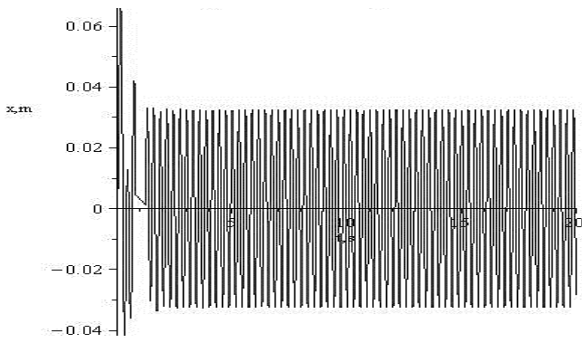


Figure 3 Graph of displacement x against t .

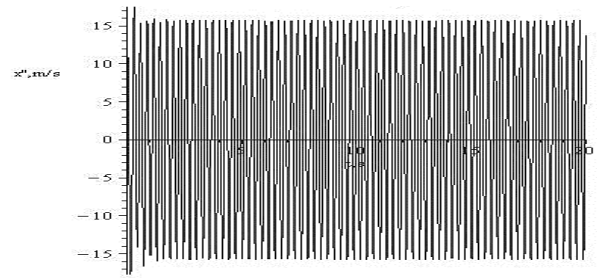


Figure 4 Graph of acceleration \ddot{x} against t .

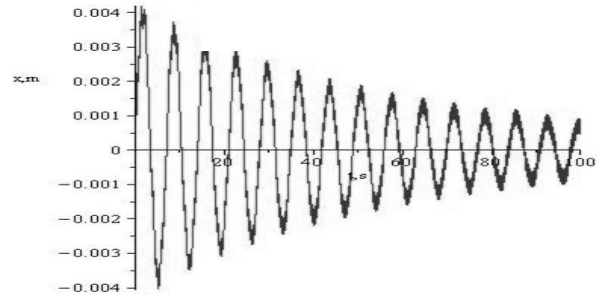


Figure 5 Graph of displacement x against t .

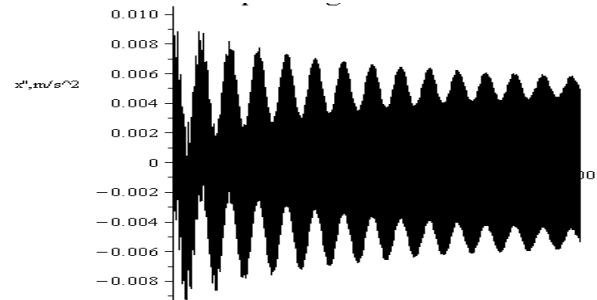


Figure 6 Graph of acceleration \ddot{x} against t .

4. CONCLUSION

In conclusion, the examine of car suspension system on sinusoidal road profile reveals that the refinement car model by adding axle and wheel to the simple car shows that it is fulfilled the prediction for both elements of displacement and acceleration. Thus, proven that refined car model will give a better comfortable compared to simple car model.

REFERENCES

- [1] Jayachandran, R., & Krishnapillai, S. (2013). Modeling and optimization of passive and semi-active suspension systems for passenger cars to improve ride comfort and isolate engine vibration. *Journal of Vibration and Control*, 19(10), 1471-1479.
- [2] Jha, S. N., Banarjee, S., & Jain, N. (2013). *A Textbook of Automobile Technology for Class IX (Level 1)*. Goyal Brothers Prakashan.

Performance and emissions characteristics of gasoline engine fueled with octane booster-gasoline blends

Hazim Sharudin¹, Nik Rosli Abdullah^{2,*}, Mohd Fahmi Aiman Abdul Rashid², Arif Pahmi¹, M. Ridzuan Arifin¹, Mohd Fahmi Md Salleh¹

¹) Faculty of Mechanical Engineering, Universiti Teknologi MARA, Cawangan Pulau Pinang, Kampus Permatang Pauh, Jalan Permatang Pauh, 13500 Permatang Pauh, Pulau Pinang, Malaysia.

²) Faculty of Mechanical Engineering, Universiti Teknologi MARA, 40450 Shah Alam, Selangor, Malaysia.

*Corresponding e-mail: nikrosli@salam.uitm.edu.my

Keywords: Octane booster; engine performance; emission characteristic

ABSTRACT – The objective of the study was to investigate the effects of various octane booster ratio, 0.3% (OB0.3), 0.5% (OB0.5), 0.7% (OB0.7), 1.0% (OB1.0) blends with gasoline on engine performance and exhaust emissions of the 1.6-liter gasoline engine. The results show that the OB1.0 at the 2500 rpm is in lower brake specific fuel consumption value compared to the gasoline fuel by 34% at constant load 60 Nm. Besides that, the carbon monoxide and hydrocarbon produced by the OB1.0 is also lower than gasoline fuel by 22% and 0.006% respectively. In overall, the OB1.0 shows the best results for all measured parameters at all engine test conditions.

1. INTRODUCTION

The attempt at finding fuels that are cleaner than fossil fuels in combustion engine have been and continue to be done by the worldwide researchers. Referring to the research done by Cerri et al. [1] and Menezes et al. [2], a lot of studies has been carried out to understand on percentage difference of typical hydrocarbon families (olefins, aromatics, etc.) and how different compounds (ethers, etc.) can improve the knock resistance for spark ignition engine application. They are a suitable solution to increase the octane gasoline quality and ensure cleaner combustion because they contain oxygen in the molecular structure. The addition of oxygenates to gasoline can improve the fuel volatility, enhance combustion and decrease the carbon monoxide and hydrocarbon emissions, as reported by others [3,4]. In this study, octane booster is the fuel additive. Octane booster is one of the solutions that can be added to gasoline fuel which acts as corrosion inhibitors or lubricants, thus allowing the use of higher compression ratios for greater efficiency and power. Thus, in this research were studied, the main objective was to study the effects of various ratio addition of octane booster with gasoline on the engine performance and exhaust emissions.

2. METHODOLOGY

The test engine used in this study is a four cylinder spark ignition engine that can be operated in port fuel injection method. The engine is coupled with eddy current dynamometer together with the instrumentation and data acquisition system with the current research are described herein. The main function of the dynamometer coupled to the gasoline engine is to ease the process of

measurement taking of engine's torque and speed. As shown in Figure 1 is the MRU Gas Analyser VARIO Plus which is the gas analyser that is used in this experiment. This device measures the percentage of exhaust emissions such as O₂, CO₂, CO, NO_x, and HC. It has the capability to response time T90 at 30 seconds from the analyzer to the inlet, 0.05% respectively 1 ppm detection limit and both 1% FS for linearity error and repeatability.



Figure 1 MRU gas analyser VARIO plus.

In terms of its experimental procedure, high constant load (60 Nm) were applied to the engine, and the speed varies from 1500 rpm to 3000 rpm with 500 rpm as the increment. The Brake Specific Fuel Consumption (BSFC) and Brake Thermal Efficiency (BTE) were the parameters measured for the engine performance. Meanwhile, Hydrocarbon (HC), Oxides of Nitrogen (NO_x), are the exhaust emissions that were measured by the use of exhaust gas analyser. For each test fuel, the tests were carried out three times and the mean value of the data was recorded. The fuel consumption was measured as volumetric and in mass basis. During the experiment, the air pressure and surrounding temperature of the laboratory were recorded. Figure 2 shows the schematic diagram for the engine setup.

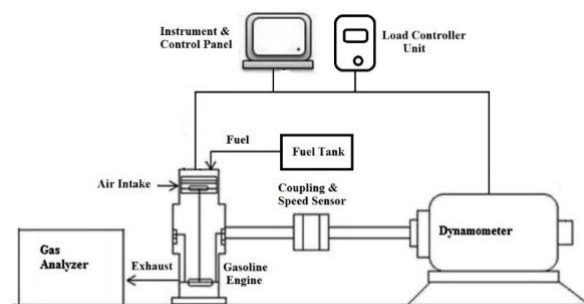


Figure 2 Schematic diagram of engine setup.

3. RESULTS AND DISCUSSION

3.1 Brake specific fuel consumption

Figure 3 shows the variations of the Brake specific fuel consumption (BSFC) of different fuel blends with respect to variations engine speeds at a constant high load of 60 Nm. The gasoline fuel possessed BSFC of 321.02 g/kWh at 2500 rpm, while the OB1.0 blend possessed BSFC of 210.5 g/kWh which is 34% lower than the gasoline fuel. It showed that OB1.0 modified blend has better BSFC than the gasoline fuel at this speed. This can be explained that as the compression ratio increases, the thermal efficiency will also be increased [4]. Thus, it will result in lower BSFC and meet fuel economy regulations.

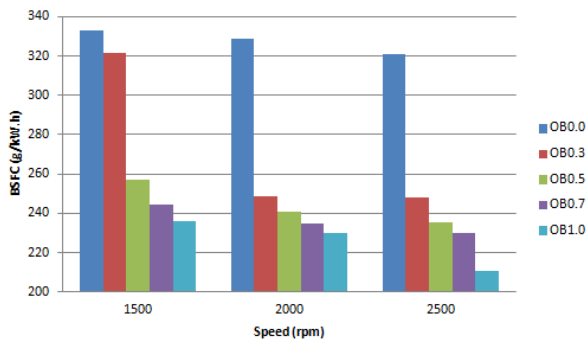


Figure 3 BSFCs vs speeds for base fuel and its modified blends at constant high load 60 Nm.

3.2 Hydrocarbon

Figure 4 shows the Hydrocarbon (HC) of the tested fuels with respect to different engine speeds at a constant high load of 60 Nm. It can be clearly seen that OB1.0 produced very low percentage of HC and cannot be measured by the gas analyser. The modified blends of OB0.3, OB0.5 and OB0.7 reduced HC than gasoline fuel on average 0.001%, 0.002% and 0.002% respectively. The reason behind this improvement is due to complete combustion is achieved. The oxygen enrichment in the fuel aids the complete combustion reaction in the internal combustion chamber [5].

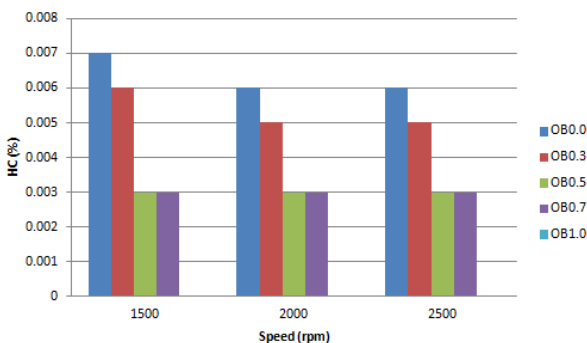


Figure 4 HCs vs speeds for base fuel and its modified blends at constant high load 60 Nm

3.3 Oxides of nitrogen

Figure 5 shows the NOx of the tested fuels with respect to different engine speeds at a constant high load of 60 Nm. The gasoline fuel exhibited lowest NOx among the other blends on average 3 ppm at 2500 rpm. This was 1 ppm lower than the all blend at the same

speed. The reason behind this improvement is due to complete combustion is achieved. The oxygen enrichment in the fuel aids the complete combustion reaction in the internal combustion chamber [6]. In conclusion, OB1.0 at 1500 rpm for 60 Nm load produced highest ppm value which is 19 ppm compared to other blends for all speed.

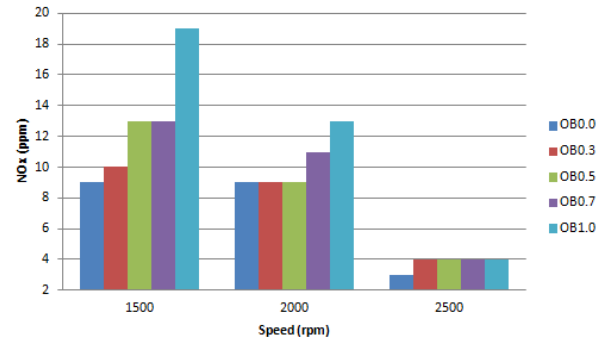


Figure 5 NOx vs speeds for base fuel and its modified blends at constant high load 60 Nm.

4. CONCLUSION

The impact of octane booster on engine performance and emissions in a spark ignition engine has been explored. For the engine experimentation, the engine performance parameters, BSFC, and emissions, NOx, and HC were measured. The results show that the octane booster able to reduce BSFC and reduce HC emissions. Therefore, it can be concluded that octane booster aids the reducing fossil fuel and environmental pollution.

REFERENCES

- [1] Cerri, T., D'Errico, G., & Onorati, A. (2013). Experimental investigations on high octane number gasoline formulations for internal combustion engines. *Fuel*, 111, 305-315.
- [2] De Menezes, E. W., Cataluña, R., Samios, D., & Da Silva, R. (2006). Addition of an azeotropic ETBE/ethanol mixture in eurosuper-type gasolines. *Fuel*, 85(17-18), 2567-2577.
- [3] Huang, Z., Miao, H., Zhou, L., & Jiang, D. (2000). Combustion characteristics and hydrocarbon emissions of a spark ignition engine fueled with gasoline-oxygenate blends. *Proceedings of the Institution of Mechanical Engineers, Part D: Journal of Automobile Engineering*, 214(3), 341-346.
- [4] Christensen, E., Yanowitz, J., Ratcliff, M., & McCormick, R. L. (2011). Renewable oxygenate blending effects on gasoline properties. *Energy & Fuels*, 25(10), 4723-4733.
- [5] Demirbas, A., Balubaid, M. A., Basahel, A. M., Ahmad, W., & Sheikh, M. H. (2015). Octane rating of gasoline and octane booster additives. *Petroleum Science and Technology*, 33(11), 1190-1197.
- [6] Cerri, T., D'Errico, G., & Onorati, A. (2013). Experimental investigations on high octane number gasoline formulations for internal combustion engines. *Fuel*, 111, 305-315.

Study on fuel characterization of methanol-ethanol additive in gasoline blends

Hazim Sharudin¹, Nik Rosli Abdullah^{2,*}, Fairuza Shahira², M. Hazimi Ismail¹, N.I. Ismail¹, A.S. Abdullah¹

¹) Faculty of Mechanical Engineering, Universiti Teknologi MARA, Cawangan Pulau Pinang, Kampus Permatang Pauh, Jalan Permatang Pauh, 13500 Permatang Pauh, Pulau Pinang, Malaysia.

²) Faculty of Mechanical Engineering, Universiti Teknologi MARA, 40450 Shah Alam, Selangor, Malaysia.

*Corresponding e-mail: nikrosli@salam.uitm.edu.my

Keywords: Fuel properties; methanol-ethanol; fuel additive

ABSTRACT – The objective of this experiment is to investigate the properties of the base fuel (100% gasoline) and blended fuels (EM3, EM7, EM10, EM15) such as density, kinematic viscosity, and lower calorific value by following ASTM test methods. The results of fuel properties show that blend EM15 have the highest density, kinematic viscosity, which were 0.95%, and 0.91%, compared with base fuel. Besides that, blend EM15 have the lowest LHV which is 6.50% lower than base fuel. This study gives a significant result that shows the blending of gasoline with alcohols lead to changes in several fuel properties which improved the engine performance and exhaust emission.

1. INTRODUCTION

The automotive sector has been thought of as a key factor in the growth of economics whether in Malaysia or global. With these rapid developments, the demand for fossil fuel is escalating and thus gives a serious effect on its sources. Due to these, researchers, institutions and industries are forced to find and discover fuel alternatives to encounter these problems. Alcohol has been identified as one of the possible alternative fuels because they can be acquired from both natural and manufactured sources [1-2]. Moreover, alcohol can be produced from renewable resources and give better engine performance with clear emission has attracted many interests on the market [3-4]. One of the attractive alcohol fuels for transportation sector is methanol and ethanol fuels due to its abundances, as well as attractive physical and chemical properties. However, only a few researches emphasize that fuel properties have played a vital role in increasing the performance of engine as well as reduce the exhaust emission because it defines the quality of the fuel [4-5]. Ethanol and methanol have some properties that permit them to be used as an additive to gasoline in internal combustion engines without any modification. These properties can directly affect the performance and emissions of the engine. The objective of this research is to study is to compare the variation of fuel properties in each different ratios of blended fuels. The scope of fuel properties covered in this research is density, kinematic viscosity, and lower heating value. The effect of these fuel properties on engine performance and exhaust emission also being identified.

2. METHODOLOGY

2.1 Blends preparation

In this study, a test matrix has been prepared which consisting of total five set of test samples that will be used for the fuel properties measurements as shown in Table 1. The matrix consists of base fuel as a reference fuel that will be compared with other blended fuels. It is noted that for each fuel blends, the total amount accounted for 100% volume percentage is equal to 1000 ml of fuel. For an example, EM3 consists of 1.5% Ethanol, 1.5% Methanol and 97% of gasoline. The blends of ethanol-methanol-gasoline were prepared by using an electrical magnetic stirrer. Besides that, the blending process was done at a low rate of stirring. The mixture of ethanol-methanol-gasoline was stirred constantly for about 15-20 minutes. For each blended fuels, this step is necessary.

Table 1 Fuel test samples (by volume).

Blended fuel	Gasoline	Ethanol	Methanol
Base fuel	100%	0%	0%
EM3	97%	1.5%	1.5%
EM7	93%	3.5%	3.5%
EM10	90%	5%	5%
EM15	85%	7.5%	7.5%

2.2 Fuel properties test

In engine testing, fuel properties measurement is necessary in order to identify each of the fuel blends characteristics that can influence engine performance and emissions. Thus, in this study, the fuel properties measurements were done in a laboratory under controlled temperatures and humidity in order to ensure accuracy. The density and kinematic viscosity were determined by using a density meter and kinematic viscosity bath based on the ASTM D4052 and ASTM D445. Meanwhile, the lower heating value was measured by using a bomb calorimeter based on the ASTM D240. For each collected data, a set of 5 experiment results for every test was averaged.

3. RESULTS AND DISCUSSION

3.1 Density

Fuel density has an important effect on engine combustion characteristics and fuel efficiency of fuel atomization. Figure 1 shows that base fuel has the lowest value of density, which is 740 kg/m³, and EM15 shows the highest density with the value of 747 kg/m³. It is also can be observed that EM3, EM5, EM10 and EM15 is increasing with the increment of 0.14%, 0.41%, 0.54% and 0.95% compared to base fuel. The increases in fuel density will cause higher fuel mass injection which will increase the fuel consumption. The changes in density will lead to differences in mass of fuel injected.

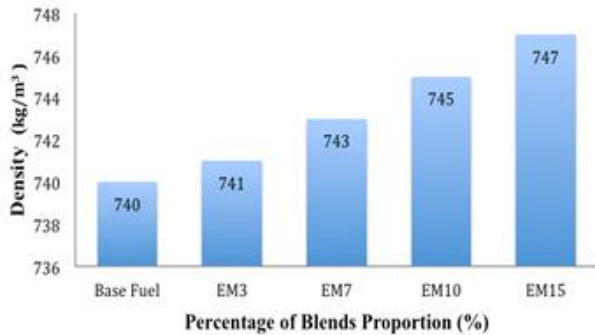


Figure 1 Variation of density.

3.2 Kinematic viscosity

Viscosity is one of the important properties because it affects the behaviour of fuel injection as an accurate amount of fuel is needed for injection. Figure 2 shows that base fuel has the lowest value of kinematic viscosity, which is 0.55 mm²/s. EM15 has the highest kinematic viscosity with 10.91% increment compared to base fuel. For blend EM3, EM5 and EM10, the increase of kinematic viscosity was about 1.82%, 3.64% and 7.27% compared to base fuel. Higher kinematic viscosity will cause higher energy needed to pump the fuel and also will increase the fuel consumption. The higher kinematic viscosity of the fuel will reduce wearing of the moving parts in engine parts and fuel systems.

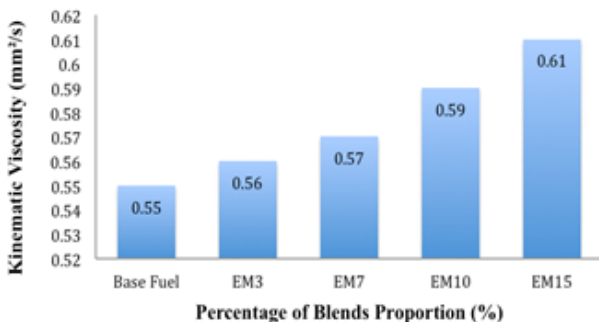


Figure 2 Variation of kinematic viscosity.

3.3 Lower heating value

The lower heating values (LHV) are known as a direct measurement of the energy content of a fuel. Figure 3 shows that base fuel has the highest LHV with the value of 43.25 MJ/kg. EM15 has the lowest value of LHV, which is 40.44 MJ/kg. The LHV of all the blended fuels shows reduction with 1.29%, 3.79%, 5.73% and

6.50%, compared to pure gasoline. The use of a fuel that has lower LHV will cause lower heat released by the combustion process. Lower heat release will require greater fuel supply in order to produce the same heat energy output as gasoline [5]. This complication will cause increases in fuel consumption of the engine.

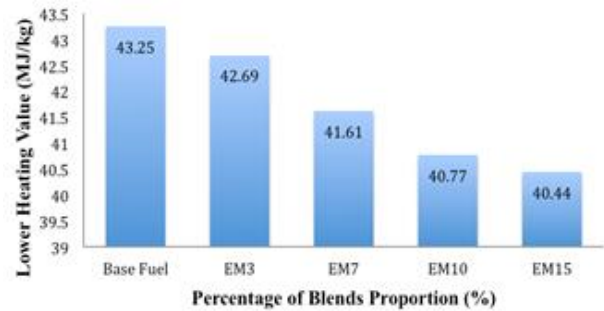


Figure 3 Variation of Lower Heating Value.

4. SUMMARY

In this study, the fuel properties of ethanol-methanol-gasoline blended fuels were determined on several fuel samples to investigate the fuel properties of these blends. The measured fuel properties are density, kinematic viscosity and lower heating value. From the results obtained, the blending of ethanol and methanol with gasoline has enhanced the fuel properties of the blended fuels. The blending of ethanol and methanol with base fuel has resulted in higher density and kinematic viscosity. Meanwhile, the lower heating value of the blended fuels is reduced. Besides that, all the values obtained by the addition of alcohol (ethanol and methanol) into gasoline are still within the range of the standards specified (EN228). Further research is required on the investigation of commercially available spark ignition engine using the improved ethanol-methanol gasoline blended fuels.

REFERENCES

- [1] Nigam, P. S., & Singh, A. (2011). Production of liquid biofuels from renewable resources. *Progress in Energy and Combustion Science*, 37(1), 52-68.
- [2] Gill, S. S., Tsolakis, A., Dearn, K. D., & Rodríguez-Fernández, J. (2011). Combustion characteristics and emissions of Fischer-Tropsch diesel fuels in IC engines. *Progress in Energy and Combustion Science*, 37(4), 503-523.
- [3] Cairns, A., Zhao, H., Todd, A., & Aleiferis, P. (2013). A study of mechanical variable valve operation with gasoline-alcohol fuels in a spark ignition engine. *Fuel*, 106, 802-813.
- [4] Balki, M. K., Sayin, C., & Canakci, M. (2014). The effect of different alcohol fuels on the performance, emission and combustion characteristics of a gasoline engine. *Fuel*, 115, 901-906.
- [5] Sharudin, H., Abdullah, N. R., Mamat, A. M., Ali, O. M., & Mamat, R. (2015). An overview of spark ignition engine operating on lower-higher molecular mass alcohol blended gasoline fuels. *Jurnal Teknologi*, 76(5), 101-105.

The control scheme of vehicle steer by wire system by using hybrid single input fuzzy logic controller and PID controller

Mohd Zaidi Mohd Tumari^{1,2,*}, Wan Norhisyam Abd Rashid¹, Ab Wafi Ab Aziz^{1,2}, Shahrizal Saat¹, Mohd Helmi Suid³

¹⁾ Faculty of Engineering Technology, Universiti Teknikal Malaysia Melaka, Hang Tuah Jaya, 76100 Durian Tunggal, Melaka, Malaysia.

²⁾ Centre for Robotics and Industrial Automation, Universiti Teknikal Malaysia Melaka, Hang Tuah Jaya, 76100 Durian Tunggal, Melaka, Malaysia.

³⁾ Faculty of Electrical and Electronics, Universiti Malaysia Pahang, 26600 Pekan, Pahang, Malaysia.

*Corresponding e-mail: mohdzaidi.tumari@utem.edu.my

Keywords: SIFLC; PID controller; vehicle steer by wire

ABSTRACT – The elimination of mechanical link between the steering wheel and front wheel of Vehicle Steer by Wire (VSBW) system makes the traditional model-based control techniques complex and difficult to synthesize in practice. This paper presents investigations of hybrid single input fuzzy logic controller (SIFLC) and PID controller for directional control and wheel synchronization of a VSBW system. The SIFLC reduces the conventional two-input FLC (CFLC) to a single input single output (SISO) controller. The implementation environment is developed within Matlab/Simulink software for evaluation of performance in terms of input tracking capability, wheel synchronization and time response specifications.

1. INTRODUCTION

The newest technology of VSBW system has guaranteed important enhancement in vehicle safety, stability, dynamics, manoeuvrability and comfort. Because of complete separation between steering wheel and the front wheels gives the practical problems for steering control especially on directional control and wheel synchronization of vehicle. A considerable amount of literature has been published on VSBW control system. These studies include PID controller [1,2], Linear-quadratic regulator (LQR) [3] and adaptive global fast sliding mode control (AGFSMC) [4]. Furthermore, several attempts have been made to control the VSBW system by using Fuzzy logic controller such as in [5]. Nevertheless, the implementation of Fuzzy logic controller requires a large amount of design effort to tune the membership functions. This paper presents the development of hybrid single input fuzzy logic controller (SIFLC) and PID control scheme for VSBW system. The SIFLC is a simplification of the conventional FLC (CFLC) by letting the system to be SISO. A considerable amount of literature has been published on SIFLC for various application such as in [6,8,9,10]. The simulation work is developed within Matlab/Simulink software for performance evaluation of the control scheme.

2. CONTROLLER DESIGN

The block diagram of the VSBW system is shown in Figure 1. The input for the system is a torque driver, T_{driver} . The motor torque, T_{M1} and torque friction, T_{fric} act as a disturbance to the system. SIFLC is responsible to compensate the error produced by steering wheel angle, θ_{sw} . Then, θ_{sw} is fed to the input of the front wheel system. The PID controller in front wheel system will control the wheel displacement, δ_f to operate the system according to the input.

SIFLC is succeeded by applying the signed distance method [7] where the input to SIFLC is only one variable known as “distance”. This is difference to the CFLC which requires an error and the derivative error as its inputs. The reduction in the number of inputs simplifies the rule table to one-dimensional, letting it to be a single input single output (SISO) controller. Thus, it can be a practical controller for VSBW system.

The structure of SIFLC derived from the signed distance method can be illustrated as a block diagram in Figure 2. Two system state variables e (error) and \dot{y} (velocity) are selected as the feedback signal. The input to the FLC block is the distance variable d , while the output from FLC block is the change of control output \dot{u}_0 . The final output of this SIFLC is obtained by multiplying \dot{u}_0 with the output scaling factor, denoted as r . The output equation can be written as in Equation (1).

$$u = \dot{u}_0 r \quad (1)$$

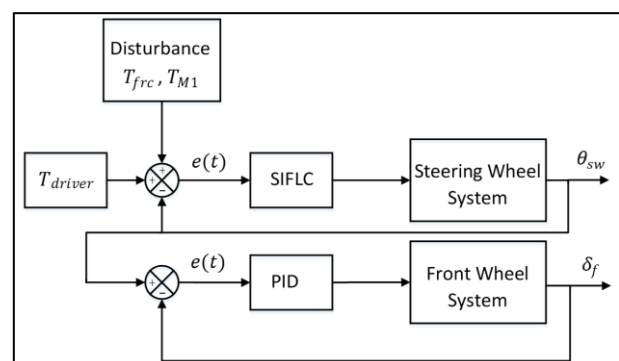


Figure 1 Block diagram of VSBW system.

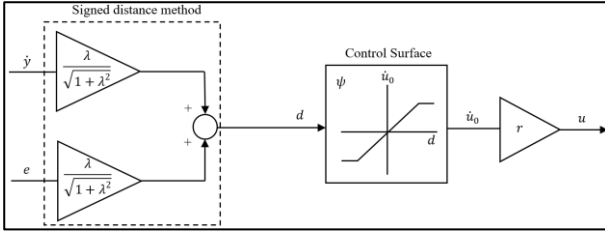


Figure 2 SIFLC structure for VSBW system with linear control surface.

3. RESULTS AND DISCUSSION

To prove the efficacy of the proposed control scheme, the steering wheel and front wheel model in [1] which consists of two dc motors is considered. Performance of the Hybrid SILC and PID is compared with PID-PID as published in [1]. The PID controller parameters are tuned by using manual heuristic tuning based on time response behavior. Figure 3 shows the step response for steering wheel angle and front wheel angle. The result of SIFLC-PID shows that steering wheel angle can track the desired T_{driver} with zero steady state error and no overshoot compared to PID-PID controller with overshoot about 10%.

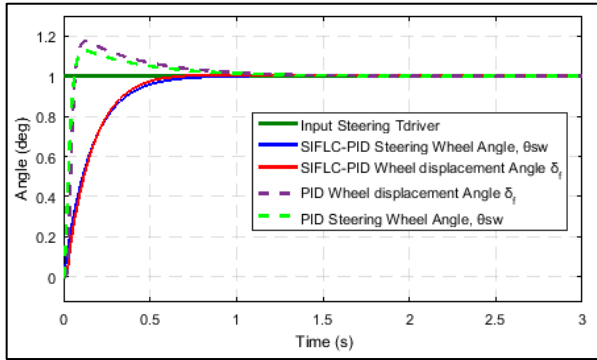


Figure 3 Step response for θ_{sw} and δ_f for SIFLC-PID and PID-PID.

For SIFLC-PID, the front wheel displacement angle can track the steering wheel angle well with zero steady state error and no overshoot which is far better than PID-PID that produced the overshoot about 19%. Both controllers have an identical settling time, T_s which is less than 1 second. But the rise time for PID-PID is faster than SIFLC-PID.

To test the reliability and robustness of the controller, the motor torque, T_{M1} and torque friction, T_{frc} were applied to the system to react as a disturbance. In Matlab/Simulink, the random real-number between [0 1] is used as a disturbance for the system. Figure 4 shows the step response for steering wheel angle and front wheel angle with disturbance. The results indicate that the system with SIFLC-PID produces a better response compared to PID-PID. For SIFLC-PID, the steering wheel angle is able to track the desired input without overshoot and steady state error, but for the front wheel angle, it has a little overshoot about 10%. Meanwhile, the system with PID-PID, both steering wheel and front wheel angle can track the desired input but unable to settles with maximum residual of $\pm 0.15^\circ$.

The system is tested with another signal which is sinusoidal input to test the repetitive operation. Figure 5

shows the results for steering wheel angle and front wheel angle with sinusoidal input. From the result, it clearly shows that SIFLC-PID produced better response which is it can track the desired input with minimal error about 0.04° compared to PID-PID, 0.1° .

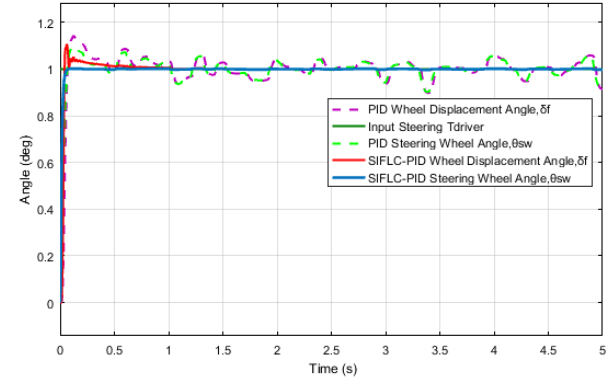


Figure 4 Step response for θ_{sw} and δ_f for SIFLC-PID and PID-PID with disturbance.

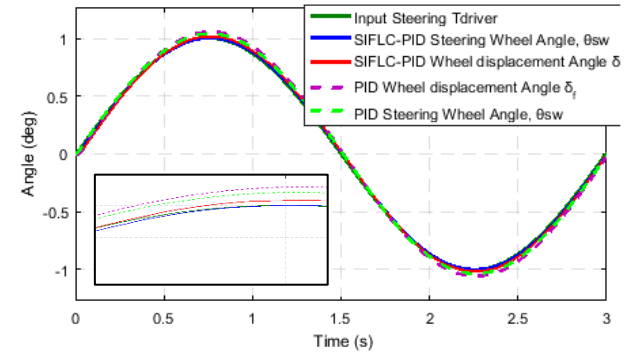


Figure 5 Sinusoidal response for θ_{sw} and δ_f for SIFLC-PID and PID-PID.

4. CONCLUSION

Investigations into directional control and wheel synchronization of a VSBW system using the hybrid SIFLC and PID controller have been presented. The proposed control schemes have been implemented and tested within simulation environment of a VSBW system. The performances of the control schemes have been evaluated in terms of input tracking capability, wheel synchronization and time response specifications. The implementation of SIFLC requires less of design effort to tune the membership functions compared to CFLC. Finally, it is concluding that the SIFLC-PID controller is capable to improve the performance of VSBW system.

ACKNOWLEDGEMENT

This work was supported by Faculty of Engineering Technology, Universiti Teknikal Malaysia Melaka, especially Robotic, Industrial and Automation (RIA) Research Group under research grant PJP/2018/FTK (10B)/S01610.

REFERENCES

- [1] Tumari, M. Z. M., Saealal, M. S., Rashid, W. N. A., Saat, S., & Nasir, M. A. M. (2017). The vehicle steer by wire control system by implementing PID Controller. *Journal of Telecommunication*,

- Electronic and Computer Engineering*, 9(3-2), 43-47.
- [2] Tumari, M. Z. M., Nasir, M. A. M., Saealal, M. S., Aziz, A. W. A., Saat, S., Suid, M. H., & Ghazali, M. R. (2017). The control scheme of vehicle steer by wire system by using PD-PID controller. *Proceedings of Mechanical Engineering Research Day 2017, 2017*, 13-14.
 - [3] Aly, M., Roman, M., Rabie, M., & Shaaban, S. (2017). Observer-based optimal position control for electrohydraulic steer-by-wire system using gray-box system identified model. *Journal of Dynamic Systems, Measurement and Control, Transactions of the ASME*, 139 (12), Article No. 121002.
 - [4] Iqbal, J., Zuhair, K. M., Han, C., Khan, A. M., & Ali, M. A. (2017). Adaptive global fast sliding mode control for steer-by-wire system road vehicles. *Applied Sciences*, 7(7), Article No. 738.
 - [5] Yuan, Z., & Wang, R. (2017). Coordinated control for vehicle handling and stability: A fuzzy robust approach. *29th Chinese Control and Decision Conference, China, 2017*, 6325-6330.
 - [6] Ghazali, M. R., Ibrahim, Z., Suid, M. H., Saealal, M. S., & Tumari, M. Z. M. (2016). Single input fuzzy logic controller for flexible joint manipulator. *International Journal of Innovative Computing, Information and Control*, 12(1), 181-191.
 - [7] Choi, B. J., Kwak, S. W., & Kim, B. K. (2000). Design and stability of single-input fuzzy logic controller. *IEEE Trans. Syst. Man Cybern., Part B, Cybern*, 30(2), 303-309.
 - [8] Tiwari, K.N., Waghmare, L.M. and Krishnankutty, P. (2016). Single input fuzzy logic controller tuning for steering control of autonomous underwater vehicle: Genetic algorithm approach. *IEEE Int Control Conference (ICC), 2016 Indian*, 335-340.
 - [9] Ahmad, M.A., Saealal, M.S., Ismail, R.R., Zawawi, M.A., Nasir, A.N.K. and Ramli, M.S. (2011). Single input fuzzy controller with command shaping schemes for double-pendulum-type overhead crane. *Int AIP conference proceedings*, 1337(1), 113-117.
 - [10] Aras, M.S.M., Abdullah, S.S. and Azis, F.A. (2015). Review on auto-depth control system for an unmanned underwater remotely operated vehicle (ROV) using intelligent controller. *Journal of Telecommunication, Electronic and Computer Engineering*, 7(1), 47-55.

Extreme condition strain signal reliability assessment using empirical mode decomposition

N.N.M. Nasir*, S. Abdullah, S.S.K. Singh, S.M. Haris

Centre for Integrated Design for Advanced Mechanical System (PRISMA), Faculty of Engineering and Built Environment, Universiti Kebangsaan Malaysia, 43600 UKM Bangi, Selangor, Malaysia

*Corresponding e-mail: nadiananasir13@gmail.com

Keywords: Empirical mode decomposition; Gumbel distribution; strain data

ABSTRACT – This paper studies the reliability of the decomposition strain signal data using the Gumbel distribution model. The fatigue signal is decomposed using the Hilbert-Huang transform method, Empirical Mode Decomposition, which extracted a set number of intrinsic mode functions that emphasized a different oscillation with different amplitudes and frequencies. Each decomposition signal is calculated with Gumbel distribution to identify the decomposition signal data characteristics. The decomposition process produced 9 IMFs and a residue showing the pattern of PDF and CDF for each IMF signal.

1. INTRODUCTION

The empirical mode decomposition (EMD) method is commonly applied in engineering fields because it is intuitive, direct and adaptive. The signal processing was suitable for non-linear and non-stationary, based on local time scale data characteristics [1].

Gumbel distribution model uses log-Weibull distribution, which is useful for estimating natural extreme phenomena and the behaviour of the signal itself. The Gumbel distribution is important due to its extreme value behaviour.

2. METHODOLOGY

This work uses the strain signal of rural road conditions which records over 60 seconds (as shown in Figure 1). The signal collected using the test road which the strain gauge was attached to the coil spring of a sedan car. This part was the highest stress location and was obtained through finite element analysis. The sampling frequency was determined to be 500 Hz with 30,000 data points.

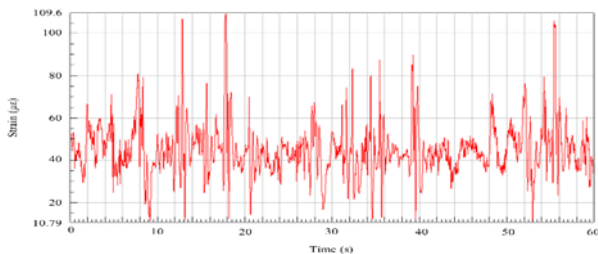


Figure 1 Strain signal of rural roads.

An empirical algorithm, namely the EMD method, was used to describe non-linear and non-stationary signals. It was developed to avoid the deficiencies of the traditional method. EMD is mainly used in Hilbert-Huang transform, which decomposes signals into finite

and set functions called intrinsic mode functions (IMFs). IMF should be a zero-mean oscillation signal that satisfies two conditions: 1) number of extrema and number of zero crossings; which are either equal to or different by at most one, and 2) at any point, the mean value of the envelope is defined by the local maxima and the envelope is defined by the local minima in zero. EMD extracts the IMF in the following sifting step:

- i. Identify the local maxima and minima of $x(t)$.
- ii. Determine upper and lower envelopes using cubic spline interpolation of the extrema point.
- iii. Calculate mean $m(t)$ as the average of upper and lower envelopes.
- iv. Compute $h(t) = x(t) - m(t)$.
- v. If the sifting result $h(t)$ is an IMF, then stop. Treat as signal $h(t)$ and iterate through steps i-v. The stopping condition is as follows:

$$\sum_i \frac{[h_{k-1}(t) - h_k(t)]^2}{h_{k-1}^2(t)} < SD \quad (1)$$

where $h_k(t)$ is the sifting result in the k^{th} iteration, SD is the standard deviation of the IMF and typically sits between 0.2 and 0.3 to make the criterion more stable [2].

Gumbel distribution is the reliability model with two parameters, location (μ) and scale (β) parameter. The random variable (x) follows Gumbel model with location $-\infty < \mu < \infty$ and scale $\beta > 0$ parameter, respectively. The probability density function (PDF) is shown as follows,

$$f(x; \mu, \beta) = \frac{1}{\beta} e^{\frac{x-\mu}{\beta}} e^{-\frac{x-\mu}{\beta}} \quad (2)$$

The corresponding cumulative distribution function (CDF) is

$$F(x; \mu, \beta) = e^{-e^{\frac{x-\mu}{\beta}}} \quad (3)$$

3. RESULTS AND DISCUSSION

The original rural road signal was decomposed into IMFs based on the HHT algorithm. From the results, the IMF described the pressure fluctuations from high to low frequencies by expressing the filtering properties of EMD. The frequency value of each IMF is shown in Table 1. Each signal shows that the frequency value decreased because the component remained as a monotonic function with one extreme point. From the beginning of decomposition, the signal amplitude changed from high to low, until the decomposed signal was completed. The two IMFs (IMF 1 and IMF 2) were

real components of the signal that were still in the high-frequency range; whereas the others were in the low frequency range (IMF 3 until IMF 9).

Each IMF component was recognised as an adaptive basis function. Figure 2 shows the signal that was decomposed into 9-component IMFs and residue of the original signal. IMF is a function of time and amplitude and indicates a unique time-frequency characteristic. EMD has its own characteristics as follows: 1) EMD decomposes the multi-component signal into a number of component signals, which is the purpose of EMD; 2) EMD decomposes the signal into several IMFs that meet the integrity and orthogonal conditions; 3) EMD decomposes the signal following the signal itself and the number of IMFs is finite. Meanwhile, the residue shown in Figure 2 appeared and became monotonic; sifting stopped, and no more IMFs were extracted.

Table 1 Frequency (Hz) range of the IMFs.

IMF	1	2	3	4	5
Frequency	30.12	4.83	2.20	1.02	0.52

IMF	6	7	8	9
Frequency	0.28	0.15	0.07	0.03

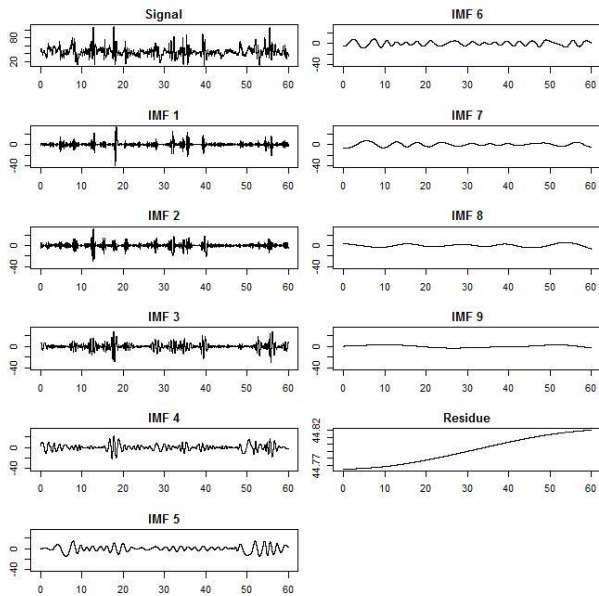


Figure 2 The empirical mode decomposition of rural road signals.

Gumbel distribution was developed to govern the load as a measurement of duration of the failure process. The data shown in Figure 3 is the probability density function (PDF) and in Figure 4, the cumulative distribution function (CDF). The Figure 3 shows that the pattern of decomposition signal for PDF was skew to the left which represents the maximum extreme values. This distribution had very long-tailed and bounded from negative to zero. While CDF in Figure 4 represent the decomposition, signal was falling between zero and one. It increases from the smallest to the largest value of CDF. The shape of the Gumbel model is skewed on one

peak ranging from 0 to 5. Kumar et al. [3] mentioned that the PDF shifts to the left if the μ decreases, and if the μ increases, the PDF shifts to the right.

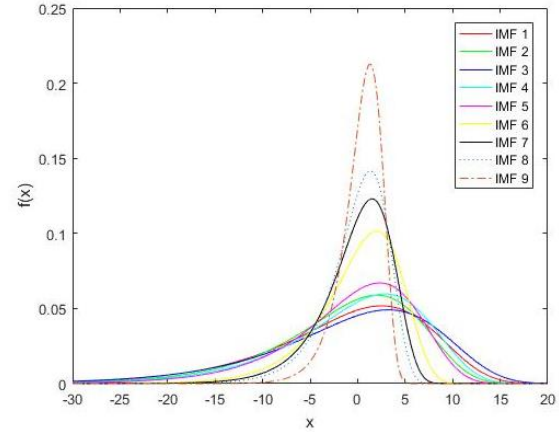


Figure 3 Probabilistic density function for decomposition signals.

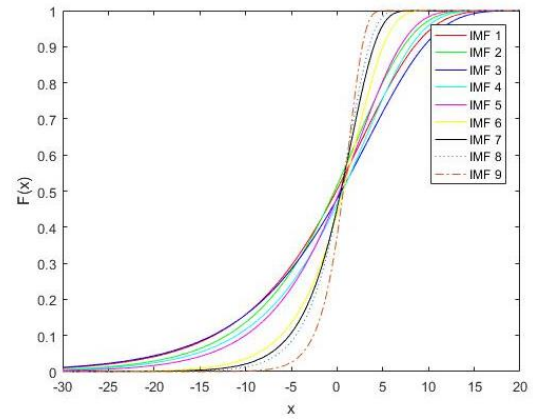


Figure 4 Cumulative distribution function for decomposition signals.

4. CONCLUSION

The EMD was used to implement the decomposition of the original fatigue data by obtaining the IMF modes to show a clear non-stationary behaviour. EMD analysis decomposed the signal into a set of natural oscillations in order to observe the different frequencies from each mode. The PDF and CDF were skewed; based on the increase or decrease of the μ value.

REFERENCES

- [1] Lozano, M., Fiz, J. A., & Jané, R. (2016). Performance evaluation of the Hilbert–Huang transform for respiratory sound analysis and its application to continuous adventitious sound characterization. *Signal Processing*, 120, 99-116.
- [2] Peng, Z., Peter, W. T., & Chu, F. (2005). An improved Hilbert-Huang transform and its application in vibration signal analysis. *Sound and Vibration*, 286(1), 187-205.
- [3] Kumar, R., Srivastava A.K., & Kumar V. (2012). Analysis of Gumbel model for software reliability using Bayesian paradigm. *International Journal of Advanced Research in Artificial Intelligence*, 1(9) 39-45.

Discrete wavelet transform method for fatigue analysis on car suspension system

A.A.A. Rahim*, S. Abdullah, S.S.K. Singh, M.Z. Nuawi

Centre for Integrated Design for Advanced Mechanical System (PRISMA),
Faculty of Engineering & Built Environment, Universiti Kebangsaan Malaysia, 43600 UKM Bangi, Selangor, Malaysia.

*Corresponding e-mail: airee.afiq@siswa.ukm.edu.my

Keywords: Discrete wavelet transform; fatigue analysis; PSD

ABSTRACT – This paper studies the significance of the discrete wavelet transform method for fatigue life analysis of car suspension systems. Issues related to time series data include how to extract important information. The strain signal is obtained under rural road conditions. The energy spectrum is obtained to extract high amplitude activities. The signal is then filtered based on the energy spectrum obtained and discrete wavelet transform method is applied. Signals from levels 1 to 7 remain similar to that of the original. The behaviour of strain signal is characterised to show the significant levels for fatigue analysis.

1. INTRODUCTION

The common method of collecting experimental data involves sequences of values at regularly spaced intervals in time; also known as time-series. The main problem is how to process them in order to extract meaningful and correct information [1]. For this reason, discrete wavelet transform (DWT) algorithms have become standard tools for processing signals in several areas of industry research. As DWT provides both octave-scale frequency and spatial timing of the analysed signal, it is constantly used to solve signal processing analyses. This work is focused on three main aspects; the energy spectrum from data generated by car suspension systems using strain gauges to determine high amplitude activities; wavelet decomposition of signals and the behaviour of each signal obtained; and the power spectral density (PSD) of the decomposed signal. Assessments are performed by comparing the damage value and the energy contained from PSD with 12 decomposition levels based on the frequency range of each signal.

2. METHODOLOGY

Figure 1 shows the location of strain gauges located on the coil spring of the car suspension system and the rural road conditions used in this study. Based on the previous research, the sampling frequency for the loading signal measurements should be greater than 400 Hz [2]. Hence, the resulting signals, which are sampled at 500 Hz are used in this study. This value seemingly suitable for the on-site data collection. Subsequently, time domain, frequency domain and time-frequency domain approaches are adopted to analyse the signals. For the time domain analysis, the strain signals are analysed by observing the behaviour and fatigue life of the signals; as determined using commercial software.

The Coffin-Manson, Smith-Watson-Topper and Morrow models are expressed in Equations (1), (2) and

(3), respectively.

$$\varepsilon_a = \frac{\sigma'_f}{E} (2N_f)^b + \varepsilon'_f (2N_f)^c \quad (1)$$

$$\sigma_{\max} \varepsilon = \frac{(\sigma'_f)^2}{E} (2N_f)^{2b} + \sigma'_f \varepsilon'_f (2N_f)^{b+c} \quad (2)$$

$$\varepsilon = \frac{\sigma'_f - \sigma_{\text{mean}}}{E} (2N_f)^b + \varepsilon'_f (2N_f)^c \quad (3)$$

Where ε_a is the true strain amplitude, σ is the fatigue strength coefficient, b is the fatigue strength exponent, ε'_f is the fatigue ductility coefficient, c is the fatigue ductility exponent, E is the Young's modulus and $2N_f$ is the number of cycle to failure. The fatigue life in the Coffin-Manson relationship was calculated based on strain amplitude at zero mean stress. SWT and Morrow models considered the mean stress effect in the calculation of fatigue life. The correction of mean stress effect of Morrow is more realistic. The fatigue damage can be calculated using Equation (4):

$$D = \frac{1}{N_f} \quad (4)$$

Where D is fatigue damage and N_f is the number of cycle to failure.

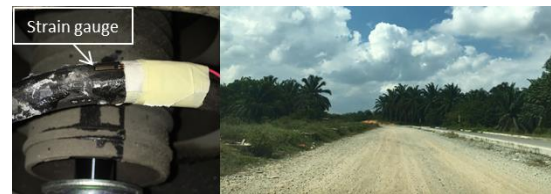


Figure 1 Position of strain gauge attached at car coil spring and type of road used.

In order to perform frequency domain analysis, the PSDs of the signals are obtained to get the energy distribution in the signals. The process includes the conversion of the time domain signal into the frequency domain. For most fatigue studies, the frequency domain analysis is done using PSD, which is a spectrum analyser that considers the energy of a signal in the frequency domain. PSD can be expressed as follows:

$$PSD = \frac{1}{2\pi} \sum_{n=-\infty}^{\infty} F(n) e^{-i\omega t} \quad (5)$$

Where F is the signal with the number of data n , t is the time and ω is the angular frequency.

Decomposition of signals was performed using

Daubechies 4th order with 12 levels of decompositions; which are the optimal levels to remove most noise. Daubechies 4th Wavelet is selected due to the similarity of its scaling function to the shape of the strain signal [3]. Wavelet decomposition calculates the group index; known as wavelet coefficient. The coefficients are obtained from the signal regression generated at different frequency scales in a wavelet [4]. The signal generated establishes the correlation between the wavelet and a section of the signal being analysed. The Daubechies wavelet transform of class $D-2N$ is a function $\varphi = N^\varphi \in L^2(\mathfrak{R})$, which is defined as follows:

$$\varphi(x) = \sqrt{2} \sum_{k=0}^{2N-1} (-1)^k h_{2N-1-k} \varphi(2x-k) \quad (6)$$

Where $h_0, \dots, h_{2N-1} \in \mathfrak{R}$ and N is the order.

3. RESULTS AND DISCUSSION

Figure 2 shows the energy spectrum of the original signal and the decomposition strain signal up to 12 levels. Based on the energy spectrum shown, there are several durations where the component experienced a high amplitude caused by uneven road surfaces and potholes. Based on the energy spectrum of the original strain signal, the filtered signal was obtained by selecting the high energy duration only. The signal can then be categorised as a signal from the original and filtered strain signals. The filtered strain signal containing high amplitude activities occurred. Therefore, the critical amplitude that leads to failure is studied in order to identify the effect of high amplitude strain signal on the component.

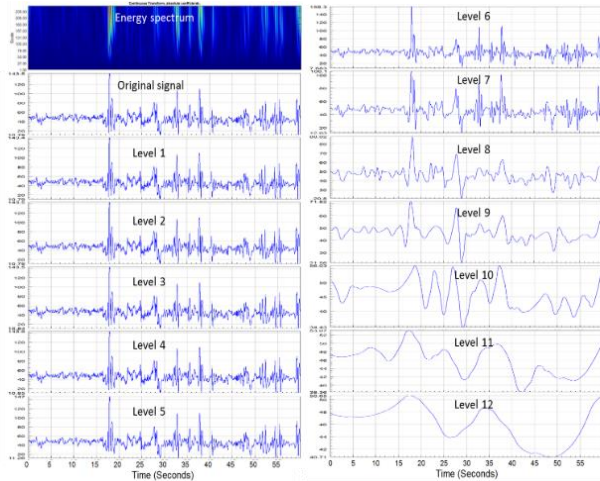


Figure 2 Energy spectrum of the original signal and decomposition strain signal up to 12 levels.

Next, the original signal is broken down into 12 levels of decomposition, in order to build the significance of DWT in a fatigue analysis study. Figure 2 also shows the results of wavelet decomposition signals using the DWT method. For each decomposed signal, the fatigue life was calculated and plotted on the graph shown in Figure 3. Based on the result obtained, the trend for number of cycles for level 1 until level 7 shows the change almost the same as the original signal which are between 10^6 to 10^7 cycles. The others levels gave higher values number of cycles which are more than 10^7 cycles.

The relationship between each level of decomposition and energy from the PSD is obtained as shown in Figure 4. Based on the results obtained, the energy contained in the PSD remains similar to that of the original signal; from level 1 to level 7. The energy from PSD for original signal and signal from level 1 to level 7 are between $2.83 \times 10^6 \mu\epsilon^2$ to $5.30 \times 10^6 \mu\epsilon^2$. In conclusion, the fatigue life and energy contained from PSD remains similar to that of the original signal; from level 1 to level 7.

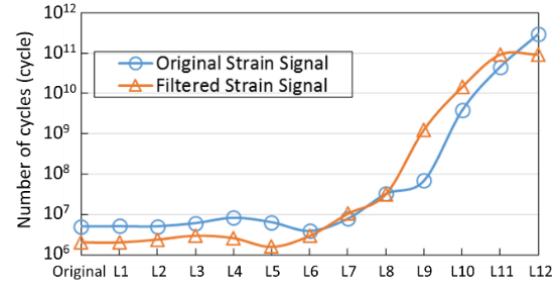


Figure 3 Number of cycles for the original and filtered strain signals for all decomposition signals.

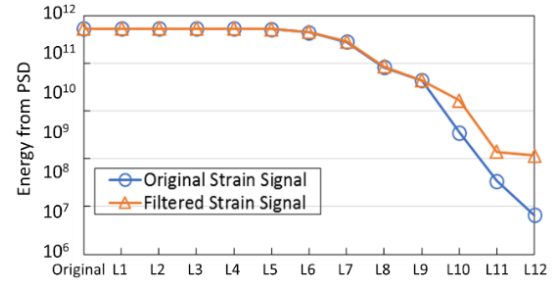


Figure 4 Energy from PSD for the original and filtered strain signals for all decomposition signals.

4. CONCLUSION

The DWT method was applied to the time series strain signal for car suspension systems and rural road conditions were selected for this study. The implementation of this method produced 12 levels of decomposition signals with the filtered signal containing a high amplitude strain signal. In conclusion, the fatigue life and energy contained from PSD remains similar to that of the original signal; from level 1 to level 7.

REFERENCES

- [1] Y. Lei, Z. He & Y. Zi. 2009. Application of the EEMD method to rotor fault diagnosis of rotating machinery. *Mechanical Systems and Signal Processing*. 23(4): 1327-1338.
- [2] M. Haiba, D. C. Barton, P. C. Brooks & M. C. Levesley. 2003. The development of an optimization algorithm based on fatigue life. *International Journal of Fatigue*. 25(4): 299-310.
- [3] A. M. Muhidin & A. D. Mohamed. 2014. An Approach for ECG Feature Extraction using Daubechies 4 (DB4) Wavelet. *International Journal of Computer Applications*. 96(12): 36-41.
- [4] R. J. Medina-Daza, N. E. Vera-Parra & E. Upegui. 2017. Wavelet daubechies (db4) transform assessment for worldview-2 images fusion. *Journal of Computers*. 12(4): 301-308.

Durability test for automobile suspension from equivalent damage modelling under constant amplitude load

R. Manouchehry Nya*, S. Abdullah, S.S.K. Singh

Centre for Integrated Design for Advanced Mechanical System (PRISMA),
Faculty of Engineering and Built Environment, Universiti Kebangsaan Malaysia,
43600 UKM Bangi, Selangor, Malaysia.

*Corresponding e-mail: r.manouchehrynia@gmail.com

Keywords: Coil spring; durability analysis; equivalent damage

ABSTRACT – This study aims to investigate equivalent damage constant amplitude for durability testing for automobile suspension systems. Coil spring is assessed via road loads in highly variable conditions. Fatigue life evaluation was investigated as a problem in ground vehicle suspension systems by creating an equivalent damage constant amplitude test from variable amplitude loading (original data). This research demonstrates that the strain life approach is an important part of whole fatigue life, because of localise plasticity. The rural, campus and highway road loads based on time strain signals were captured. The results have shown that highway areas have the highest fatigue life of 2.14×10^7 from the Smith-Watson-Topper model.

1. INTRODUCTION

Generally, coil spring suspension systems which that are connected to the body of the motor vehicle, are categorised as a safety part of automotive structures. Hence, the coil spring durability tests are essential to guarantee operation the vehicles in order to prevent of failure under service loadings [1]. Investigating the fatigue of vehicle component's vibration, especially for springs, is sensitive, because fatigue may occur under varying service loads during long periods of time. Accelerated durability tests investigated [2] via specific software to analyse the life specifications of motor vehicles for utilising common conditions at superior stress levels for acceleration in the incidence of damage. A new modifying simulation of acceleration durability tests revealed the precision more than 95% of loading profiles. F. Cianetti et al. [3] developed a durability acceleration test for dynamic components according to a method of fatigue damage spectrum (FDS). The technique revealed the efficacy of multiple loading compound conditions to an equivalent. This study introduces the strain life approaches that the original strain data is captured as a variable amplitude loading (VAL) for coil springs of motor vehicle suspension systems. The objective of this study is to consider the durability analysis to design an equivalent damage based on VAL to constant amplitude loading (CAL). The results of VAL and CAL tests can be applied to structures as a durability test.

2. METHODOLOGY

In this study, original strain time history was used based on a random loading, as well as a signal based on constant loading in different types of road loads. A coil

spring was selected for the durability analysis of a component, when subjected to VAL and CAL during road loads. The Smith-Watson-Topper (SWT) model where used to compare the results of fatigue life and damage between VAL and CAL. This research demonstrates a design equivalent damage assessment from random loadings to a constant loading for fatigue life prediction of coil springs in ground vehicle components. The Palmgren-Miner method is also known as the linear damage accumulation rule. This method is very effective in the automobile industry at calculating the fatigue damage of a structure. The linear damage accumulation rule can be determined using the sum total of partial damage as follows:

$$D = \sum_{i=1}^n \frac{n_i}{N_{f_i}} = 1$$

Where D is the accumulated damage, n_i is the number of applied cycles and N_{f_i} is the number of constant

amplitude cycles to failure. The structure is failed when the total damage reaches a value of 1. Material properties were chosen from chromium steel, SAE5160, which is frequently used in the construction of coil springs. Table 1, shows the material properties of the coil spring.

Table 1 Material properties of the SAE5160 steel [4].

Material property	Value
Yield strength(MPa)	1070
Ultimate tensile strength (MPa)	1550
Material modulus of elasticity (GPa)	207
Fatigue strength coefficient (MPa)	2063
Fatigue strength exponent	-0.08
Fatigue ductility exponent	-1.05
Fatigue ductility coefficient	9.56
Cyclic-strain hardening exponent	0.10
Cyclic strength coefficient	2000

3. RESULTS AND DISCUSSION

A coil spring is subjected to random excitations by wheels on the road. The signals are usually Gaussian and linear, which can be fundamental criteria of fatigue vibration. Figure 1, shows the plot of damage and strain time history together. According to the existing large

values of strain in the overall signal, from these two parameters the high strain value assists fatigue damage. According to figure 1, the lower fatigue damage indicated lower energy, while the higher energy belongs to high amplitudes from potential fatigue damage signals. Furthermore, the higher fatigue damage is subjected to higher energy or higher amplitude.

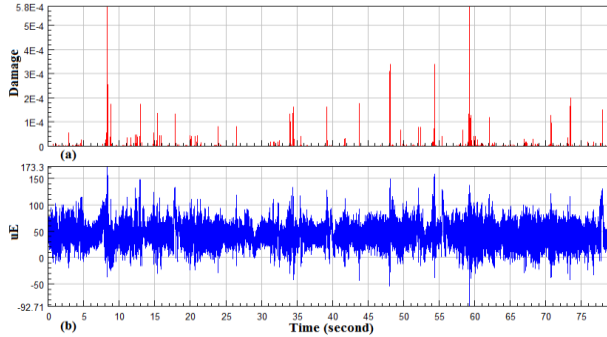


Figure 1 Plots of fatigue analysis: (a) Damage magnitude and (b) strain time history.

This research is based on a time domain approach. Therefore, the Rainflow cycle counting method and fatigue damage rule must be applied to predict fatigue life estimation. For this purpose, utilising Rainflow cycle plots and damage accumulation model can be applied based on time domain analysis.

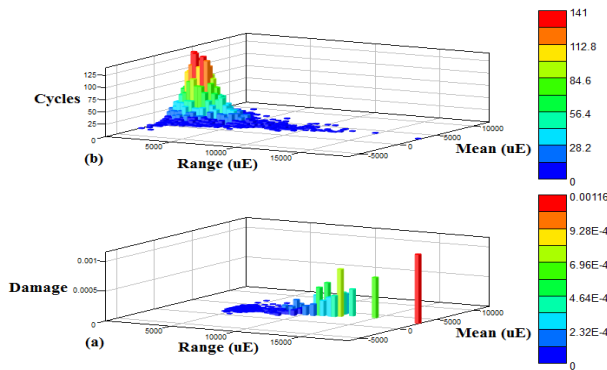


Figure 2 Histograms: (a) Cycle histogram distribution and (b) Damage histogram distribution.

Figure 2, illustrates the plots of cycle and damage histogram distribution. In this study, the SWT strain life approach is considered for the critical location of coil springs. The majority of the damage is characterised by the Rainflow cycle. Accordingly, the strain at low cycles appeared often; as shown on the left of the plot, against several cycles of high strain shown on the right. The results show that most of the damage occurred at the high strain ranges [5]. The three dimensional damage histograms provided the signal strain history (fatigue damage) distribution for each cycle as shown. Table 2, demonstrates durability results of the SWT strain life model. It made the highest fatigue life and the lowest fatigue damage for rural, campus and highway roads.

Figure 3, indicates the constant amplitude loading based on the design related to the original strain time history. This signal must be referenced to the original strain time history in the same or close to fatigue life and fatigue damage values.

Table 2 Durability results of SWT strain life model.

No	Types of road	Fatigue life	Fatigue damage
1	Rural	5.1×10^5	1.96×10^{-6}
2	Campus	2.08×10^6	4.79×10^{-7}
3	Highway	2.14×10^7	4.67×10^{-8}

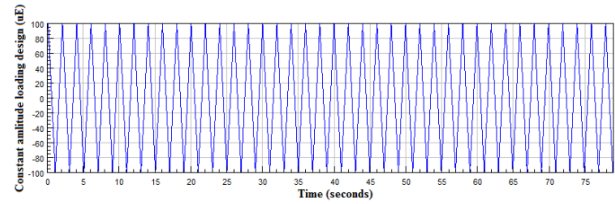


Figure 3 Constant amplitude loading strain time history.

4. CONCLUSIONS

In conclusion, this paper investigated a comparative study of total fatigue life and damage based on the SWT strain life model. VAL was modified to CAL as a repeating sine wave of single load, in order to simplify and accelerate the test. The durability results test must be equivalent or close to fatigue life and damage values. Therefore, the validation can be associated to real service use. The results presented the highest fatigue life of 2.14×10^7 and the lowest fatigue damage based on the SWT model for strain time history of highway areas.

REFERENCES

- [1] Topac, M., Ercan, S., & Kuralay, N. (2012). Fatigue life prediction of a heavy vehicle steel wheel under radial loads by using finite element analysis. *Engineering Failure Analysis*, 20, 67-79.
- [2] Xu, K., Wu, Y., & Wu, Q. (2011). Development of vibration loading profiles for accelerated durability tests of ground vehicles. In *ASME 2011 Dynamic Systems and Control Conference and Bath/ASME Symposium on Fluid Power and Motion Control*. American Society of Mechanical Engineers, 717-724.
- [3] Cianetti, F., Alvino, A., Bolognini, A., Palmieri, M., & Braccisi, C. (2018). The design of durability tests by fatigue damage spectrum approach. *Fatigue & Fracture of Engineering Materials & Structures*, 41(4), 797-796.
- [4] Karthik, J., Chaitanya, K., & Sasanka, C. T. (2012). Fatigue life prediction of a parabolic spring under non-constant amplitude proportional loading using finite element method. *International Journal of Advanced Science and Technology*, 46, 143-156.
- [5] Zakaria, K., Abdullah, S., & Ghazali, M. J. (2013). Comparative study of fatigue life behaviour of AA6061 and AA7075 alloys under spectrum loadings. *Materials & Design*, 49, 48-57.

Flapping mechanism morphological analysis for a biomimetic aerial vehicle

Siti Nur Amalina Mohd Halidi*, Ahmad Akmal Abdul Aziz, Hamid Yusoff, Aliff Farhan Mohd Yamin, Ahmad Sufian Abdullah

Faculty of Mechanical Engineering, Universiti Teknologi MARA, Cawangan Pulau Pinang, Jalan Permatang Pauh, 13500 Permatang Pauh, Pulau Pinang, Malaysia.

*Corresponding e-mail: sitinur6182@ppinang.uitm.edu.my

Keywords: Dragonfly, mechanism, biomimetic aerial vehicle

ABSTRACT – Interpreting prior studies on biomimetic aerial vehicle has led to a new design idea with improvements. This paper proposes three different mechanism designs based on these studies. Morphological chart analysis is used to determine the best mechanism based on its size, mass, material, and linkages. Solidworks is used as a tool for design study analysis. Mechanism 3 is chosen as the best design with a total wingspan of 25.62 cm and a mass of 0.0062 kg. The mechanism uses binary links for its linkages system. The proposed material used to produce the prototype is ABS (Acrylonitrile Butadiene Styrene).

1. INTRODUCTION

Biomimetic Aerial Vehicle (BAV) are a class of unmanned aircraft that mimics flapping wing kinematics of flying mechanism. In this study, dragonflies are chosen as subject of interest for biomimetic aerial vehicle. With its unique and superior flight performance, expertise in hovering condition, fast forwards and backwards, rapid turning movement and the ability to fly in sideways and accommodate gliding on water makes dragonflies the ultimate choice of subject in designing BAV. Other than that, a study by Couceiro et al. [1] stated that the wings are independently controlled based on their robust movement. As flapping are the most basic motion in many faunas, various types of flapping mechanism have been developed. Based on the robustness and complex motion of these wings, many researchers have produced design for its mechanism. Parallel crank rocker mechanism was one of the mechanism designed by Conn et al. [2] for their insect-inspired micro air vehicle. A four-bar mechanism was also developed by Khatait et al. [3] for flapping mechanism. Both mechanisms consist several linkages connecting the wings. Based on these prior design, new design ideas are currently being developed that will improve the mass, size, and linkages system.

2. METHODOLOGY

3D model of the mechanism is constructed using Solidworks. Three different types of flapping mechanisms were proposed. Mechanism 1 consists of two wings, one rotational motor and one linkage of binary links. Mechanism 2 and 3 are based from Mechanism 1 with improvements and simplifications to the mechanism. These mechanism designs were developed based on four main parameters; i.e. component size, material, mass, and linkages. Mass,

material, and size were considered based on international regulations and standards set up by FAA (Federal Aviation Administration) and EASA (European Aviation Safety Agency). Degree of Freedom (DOF) for linkages were determined by using Gruebler's equation shown on Equation (1). Six different types of linkages were considered for design construction.

$$F = 3(n - 1) - 2f_1 \quad (1)$$

Where, n is the total number of links and f is the number of joints. Once all the designs were constructed, design study analysis was conducted to ensure the optimization of the critical components of the mechanism.

3. RESULTS AND DISCUSSION

3.1 Flapping mechanism design

As mentioned in the earlier part of this paper, three different designs were made for the flapping mechanism. Mechanism 1 has the simplest design between the three mechanisms. It was designed with less complicated linkages system compared to the other two mechanisms. All three mechanisms used sliders as their main component to create movement. With its huge dimension and difficulty to fabricate parts, Mechanism 1 was not chosen. Hence modifications were made on Mechanism 1 which lead to improvised designs for Mechanism 2 and Mechanism 3. Mechanism 3 is chosen as the final design due to design failures from Mechanism 1 and Mechanism 2. Mechanism 3 design focused on minimizing the size of each components in the mechanism. Figure 1, 2, and 3 below shows the design of Mechanism 1, 2, and 3 respectively.

3.2 Morphological analysis

Morphological analysis was then conducted on all three mechanisms. Design study analysis were made to identify the optimal size, mass, and material. There were nine crucial components in Mechanism 3; i) actuator end plate, ii) ball cap, iii) blade clamp, iv) blade, v) pitch bearing housing, vi) pitch yaw coupling, vii) scotch yoke saddle, viii) yaw bearing housing, ix) yaw bearing riser. Morphological analysis was conducted on all of these components. Figure 4 below shows morphological analysis of the components in Mechanism 3.

Based on the morphological analysis, the optimal design for each of the component were determined. Table 1 shows the list of components with its optimal design from the analysis.

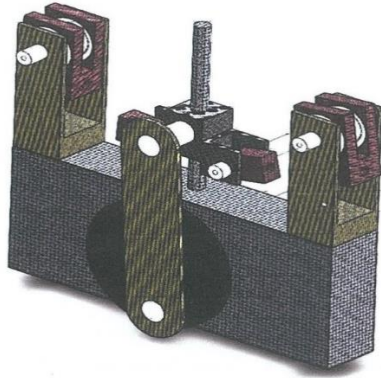


Figure 1 Design of mechanism 1.

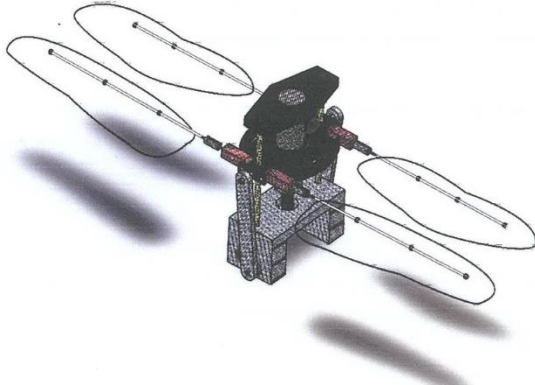


Figure 2: Design of mechanism 2.

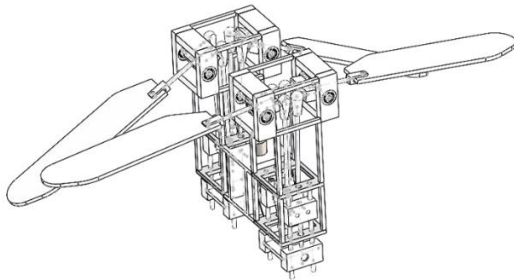


Figure 3 Design of mechanism 3.

Table 1 Optimal design number for each of the components.

No	Component	Design number
1	Actuator end plate	2
2	Ball cap	2
3	Blade clamp	1
4	Blade	1
5	Pitch bearing housing	1
6	Pitch yaw coupling	3
7	Scotch yoke saddle	3
8	Yaw bearing housing	1
9	Yaw bearing riser	5

From the analysis, by considering all prototype components to be of ABS (Acrylonitrile Butadiene Styrene) material, Mechanism 3 weighs at 62.85 grams.

ABS is chosen as material of choice for the prototype based on a previous study by Ma et al. [4] and Sivasankaran et al. [5]. ABS has higher flexibility compared to PLA and acrylic and also costs much less hence the material of choice. Not only that, the proposed Mechanism 3 design weighs 17.15 grams lighter than the prototype made by Kevin Y. Ma et al which may be useful when flying the prototype by needing less lift force than the previous prototype. Cylindrical pair, revolute pair, and spherical pair linkages were used for the design of Mechanism 3. The overall size for the mechanism is 80 mm tall, 25 mm width, and 86 mm in length. This is slightly larger than the BAV prototype made by Kevin et al as perceived since this paper based its designs from a dragonfly which has a much bigger dimension than a fly as inspired by prior studies. However, since this is only a proposed design, further improvements can be made later in the study.

4. CONCLUSION

By conducting morphological analysis and design study, Mechanism 3 is proven to be the best proposed design. At 62.85 grams, Mechanism 3 has a lighter weight than the prototype by prior studies, but with a much larger dimension. The large dimension however, is compensated by the material of choice, the ABS which proven to be much flexible to fabricate. Further improvements and modifications will then be made later in the study.

REFERENCES

- [1] Couceiro, Micael S., Nuno MF Ferreira, and JA Tenreiro Machado. "Hybrid adaptive control of a dragonfly model." *Communications in Nonlinear Science and Numerical Simulation* 17.2 (2012): 893-903.
- [2] Conn, A. T., Burgess, S. C., & Ling, C. S. (2007). Design of a parallel crank-rocker flapping mechanism for insect-inspired micro air vehicles. *Proceedings of the Institution of Mechanical Engineers, Part C: Journal of Mechanical Engineering Science*, 221(10), 1211-1222.
- [3] Khatait, J. P., Mukherjee, S., & Seth, B. (2006). Compliant design for flapping mechanism: A minimum torque approach. *Mechanism and Machine Theory*, 41(1), 3-16.
- [4] Ma, K. Y., Chirarattananon, P., Fuller, S. B., & Wood, R. J. (2013). Controlled flight of a biologically inspired, insect-scale robot. *Science*, 340(6132), 603-607.
- [5] Sivasankaran, P. N., Ward, T. A., Salami, E., Viyapuri, R., Fearday, C. J., & Johan, M. R. (2017). An experimental study of elastic properties of dragonfly-like flapping wings for use in biomimetic micro air vehicles (BMAVs). *Chinese Journal of Aeronautics*, 30(2), 726-737.



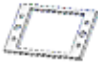


















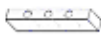


























Parts	Design 1	Design 2	Design 3	Design 4	Design 5	Design 6	Design 7	Design 8
Actuator End Plate								
Ball Cap								
Blade Clamp								
Blade								
Pitch Bearing Housing								
Pitch Yaw Coupling								
Scotch Yoke Saddle								
Yaw Bearing Housing								
Yaw Bearing Riser								

Figure 4 Morphological analysis of the components in mechanism 3.

Vehicle speed control strategy using Fuzzy-PID controller for continuously variable transmission system

Nur Rashid Mat Nuri^{1,2,*}, Khisbullah Hudha³, Saiful Amri Mazlan², Mohamad Hafiz Harun¹

¹⁾ Faculty of Engineering Technology, Universiti Teknikal Malaysia Melaka, Hang Tuah Jaya, 76100 Durian Tunggal, Melaka, Malaysia.

²⁾ Malaysia-Japan International Institute of Technology, Universiti Teknologi Malaysia Kuala Lumpur, Jalan Sultan Yahya Petra, 54100 Kuala Lumpur, Malaysia.

³⁾ Faculty of Engineering, Universiti Pertahanan Nasional Malaysia, Kem Sungai Besi, 57000 Kuala Lumpur, Malaysia.

*Corresponding e-mail: nrashid@utem.edu.my

Keywords: Vehicle speed; a Fuzzy-PID controller; continuously variable transmission

ABSTRACT – This paper presents the vehicle speed control performance using PID and Fuzzy-PID controllers in automatic and continuously variable transmissions. The longitudinal vehicle model equipped with these transmissions and controllers were simulated in MATLAB/Simulink software. The results revealed that the continuously variable transmission with Fuzzy-PID controller was performed better than an automatic transmission with PID controller in term of vehicle acceleration and able to achieve the desired vehicle speed accurately with acceptable error.

1. INTRODUCTION

Nowadays, almost all systems in vehicle is electronically controlled by electronic devices. One of the main control parameters is vehicle speed. Combination of an appropriate vehicle speed and type of transmission can lead to enhance the performance and improve the fuel economy of the vehicle [1]. Compared with manual (MT) or automatic transmission (AT), continuously variable transmission (CVT) has the capability to achieve these goals. The vehicle transmission function is to transfer the engine torque to the vehicle wheels with the desired gear ratio smoothly and efficiently.

Proportional, Integral and Derivative (PID) controller is the most practically implemented in industrial control system because of its simple structure and high reliability. Normally, the PID control strategy is determined by trial and error method or Ziegler-Nichols method. But, the PID controller parameters, the K_p , K_i and K_d are quite difficult to be fixed when the vehicle speed is changed due to external disturbances such as cross wind or road conditions. To overcome the PID controller drawbacks, the Fuzzy-PID controller is proposed which has good control characteristics especially in high nonlinear and complex vehicle system [2-3].

Thus, the aim of this study is to investigate the vehicle speed performance at different speed of 90 km/h and 110 km/h in AT and CVT by using PID and Fuzzy-PID controllers.

2. METHODOLOGY

2.1 Vehicle system model

In this study, a vehicle model in the longitudinal

direction which has two main elements, vehicle dynamics and powertrain system dynamics were used. Figure 1 shows the vehicle model structure, where the input to the model is the throttle opening setting and the vehicle speed is set as output.

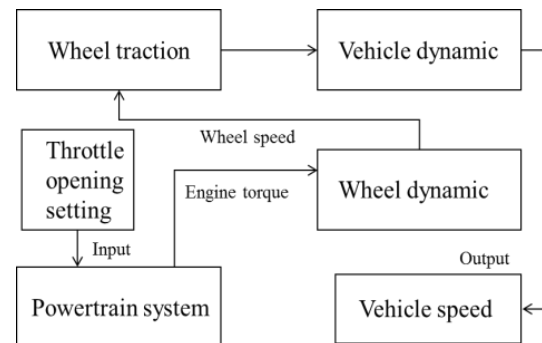


Figure 1 Longitudinal vehicle model structure.

The model structure was mathematically modelled and simulated in MATLAB/Simulink software. Table 1 shows the main parameters of the vehicle model.

Table 1 Vehicle model main parameters.

Vehicle mass	747 kg
Wheelbase	2.347 m
Height of C.G	0.54 m
Gear 1	3.78
Gear 2	2.12
Gear 3	1.36
Gear 4	1.03
Gear 5	0.84
Gear final	4.10

2.2 PID and Fuzzy-PID controllers

The PID controller is based on the proportional, integral and differential gains calculation that can be expressed on Equation (1), where $u(t)$ is controlled variable, $e(t)$ is error value, K_p is proportional gain, K_i is integral gain and K_d is a derivative gain. Then, the PID controller parameters are stated in Table 2.

$$u(t) = K_p e(t) + K_i \int_0^t e(\tau) d\tau + K_d \frac{de(t)}{dt} \quad (1)$$

Table 2 PID controller parameters.

K_p	150
K_i	0.5
K_d	5.0

On the other hand, the Fuzzy controller has been widely used because of positive characteristics such as good in robustness and strong adaptability. However, the fuzzy controller has disadvantages in term of low accuracy in the complex process. To overcome above problem, the Fuzzy-PID controller has been applied by combining the conventional PID and fuzzy controllers. The Fuzzy-PID controller used the vehicle speed error, e and vehicle speed error rate of change, ec as the inputs to the fuzzy controller. Then, the PID controller coefficients, K_p , K_i and K_d are adjusted in real time by using the fuzzy control rules. In this study, the Sugeno-type fuzzy inference was used and the structure of Fuzzy-PID controller is shown in Figure 2. The simulation was carried out for a period of 100 seconds by using *Bogacki-Shampine* solver with a step size of 0.01 second.

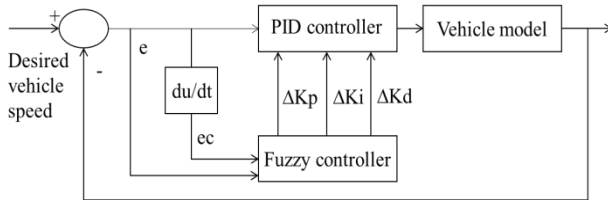


Figure 2 Fuzzy-PID controller structure.

3. RESULTS AND DISCUSSION

Figure 3 shows the vehicle speed response from 90 km/h to 110 km/h using the PID controller on the automatic transmission, PID and Fuzzy-PID controllers on CVT, respectively. It reveals that on the same PID controller, CVT has better performance in term of time taken to achieve the desired vehicle speed, less overshoot, faster time to settle and better in steady state error.

Meanwhile, the comparison between PID and Fuzzy-PID controllers on the same CVT shows that the Fuzzy-PID controller has better transient responses in term of rise time, overshoot percentage, settling time and steady state error. Detail analysis and comparison of each transmission and controller are shown in Table 3, when the vehicle needs to reach the desired speed of 90 km/h.

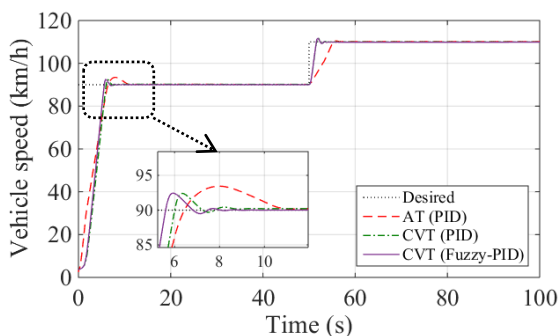


Figure 3 Vehicle speed response with different transmissions and controllers.

Table 3 Transient analysis for AT with PID controller and CVT with PID and Fuzzy-PID controllers.

Transmission (Controller)	Rise time (s)	OS (%)	Settling time (s)	Steady state error (%)
AT (PID)	6.44	3.8	12	0.24
CVT (PID)	6.00	2.7	11	0.23
CVT (Fuzzy-PID)	5.60	2.6	10	0.01

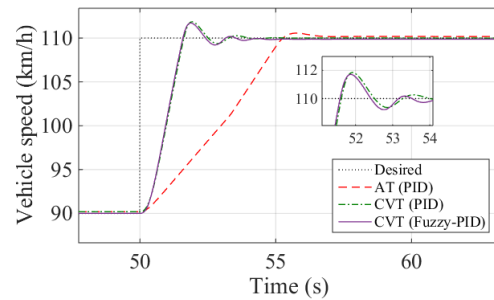


Figure 4 Zoom of vehicle speed responses when the vehicle speed increases.

Next, Figure 4 shows an enlargement view of vehicle speed responses from Figure 3 when the vehicle speed is increased to 110 km/h. In view of results obtained, the rise time to achieve desired speed is 5.25 seconds for AT, 1.62 second for CVT with PID controller and 1.58 second for CVT with Fuzzy-PID controller.

4. CONCLUSION

In conclusion, a vehicle with CVT shows better performance in term of acceleration and transient responses compared with AT. Furthermore, the vehicle speed control by Fuzzy-PID has better characteristics and good dynamic behaviour than PID, which less response time, smaller overshoot and less steady state error.

ACKNOWLEDGEMENT

This project is supported by Ministry of Education Malaysia through the research grant LRGS (LRGS/B-U/2013/UPNM/DEFENCE & SECURITY-PI).

REFERENCES

- [1] Jiang, Q., Liu, H. Y., Hao, J. J., & Cheng, Y. (2011). Ratio control strategy for an electromechanical continuously variable transmission based on engine models. *Advanced Materials Research*, 291, 2861-2865.
- [2] Zhou, Y. (2015). Fuzzy incremental PD controller design for vehicle speed control. *Robotics and Biomimetics (ROBIO)*, 440-445.
- [3] Munyaneza, O., Munyazikwiye, B. B., & Karimi, H. R. (2015). Speed control design for a vehicle system using fuzzy logic and PID controller. *Fuzzy Theory and Its Applications (iFUZZY)*, 56-61.

Prioritizing the product design specification of side-door impact beam using analytic hierarchy process method

Mohd Adrinata Shaharuzaman^{1,2,3,4}, Mohd Sapuan Salit^{1,3,*}, Muhd Ridzuan Mansor^{2,4},
Mohd Zuhri Mohamed Yusoff¹

¹⁾ Department of Mechanical and Manufacturing Engineering, Faculty of Mechanical Engineering, Universiti Putra Malaysia, 43400 UPM Serdang, Selangor, Malaysia.

²⁾ Faculty of Mechanical Engineering, Universiti Teknikal Malaysia Melaka, Hang Tuah Jaya, 76100 Durian Tunggal, Melaka, Malaysia.

³⁾ Laboratory of Biocomposite Technology, Institute of Tropical Forestry and Forest Product (INTROP), Universiti Putra Malaysia, 43400 UPM Serdang, Selangor, Malaysia.

⁴⁾ Centre for Advanced Research on Energy, Universiti Teknikal Malaysia Melaka, Hang Tuah Jaya, 76100 Durian Tunggal, Melaka, Malaysia.

*Corresponding e-mail: sapuan@upm.edu.my

Keywords: Analytic Hierarchy Process; product design specification; side-door impact Beam

ABSTRACT – Product design specification (PDS) is one of the elements in the product development process. To develop the side-door impact beam, six criteria of the PDS have been chosen and compared by ten decision makers using pairwise comparison with nine-point scale judgement by Analytic Hierarchy Process (AHP) method. Each criterion by each decision makers were sum up and the average data calculated. The average data is the result of the priority vector and it shows that the AHP can prioritize the PDS of side-door impact beam from highest to lowest which are performance, product cost, weight, environment, disposal and size.

1. INTRODUCTION

Side-door impact beam has been introduced by General Motors late in 1960's to prevent the occupants from serious injury and fatality during side impact collision [1]. Side impact collision is the second highest that cause fatality after frontal impact [2-3]. Therefore, engineers and researchers are working on to reduce the injuries and fatalities on side impact collision. Beside of the chassis and the floor that absorbed the impact energy during collision, side-door impact beam placed inside the door can reduce the intrusion to the passenger's compartment. Design requirements of the side-door impact beam should be considered from the early stage of design process, which is termed as product design specification (PDS) [4]. The PDS of side door impact beam were selected from the 32 main criteria proposed by Pugh [4] and recent research of automotive components development that considered PDS in their early stage of engineering product development [5-6]. The PDS need to be prioritize because the weightage of each criteria is different depends on the engineers, researchers, and designers. In this study, the PDS will be prioritize by ten decision makers using the pairwise comparison technique by Analytic Hierarchy Process (AHP) method to get the best weightage criteria of the PDS for side-door impact beam.

2. RESEARCH METHODOLOGY

Based on Pugh guidelines, there are six main criteria included to the side-door impact beam PDS which are i) performance (PF), ii) size (SZ), iii) weight (WG), iv) product cost (PC), v) environment (EV), and vi) disposal (DP). The PDS criteria were selected based on the recent research of automotive components which are hand brake lever [5] and automotive anti-roll bar [6].

Ten decision makers (DM) from automotive engineering and product design backgrounds were selected to evaluate the importance of each PDS criteria using AHP pairwise comparison technique. The AHP questionnaire used nine-point scale judgement as in table 1 to prioritize each of the PDS. Figure 1 shows a part of the pairwise comparison judgement for criteria number 1 which is performance (PF) compared to the other five PDS criteria.

The pairwise comparison from each decision makers were synthesized to determine the priority vector values, w using Equation (1) [7].

$$w = \frac{1}{n} \sum_{j=1}^n \frac{a_{ij}}{\sum_{i=1}^n a_{ij}}, i, j = 1, 2, \dots, n \quad (1)$$

where w is the priority vector (or eigenvector), a_{ij} is the importance scale, i.e. 1,3,5,..., and n is the number of criteria.

All the analyses were performed with the aid of Super Decisions software. Figure 1 shows the part of user interface (UI) for the software which user need to select the pairwise comparison value from the decision makers. The results for each PDS and each decision makers were recorded as in table 2.

1.PF	>=9.5	9	8	7	6	5	4	3	2	2	3	4	5	6	7	8	9	>=9.5	No comp.	2.SZ
1.PF	>=9.5	9	8	7	6	5	4	3	2	2	3	4	5	6	7	8	9	>=9.5	No comp.	3.WG
1.PF	>=9.5	9	8	7	6	5	4	3	2	2	3	4	5	6	7	8	9	>=9.5	No comp.	4.PC
1.PF	>=9.5	9	8	7	6	5	4	3	2	2	3	4	5	6	7	8	9	>=9.5	No comp.	5.EV
1.PF	>=9.5	9	8	7	6	5	4	3	2	2	3	4	5	6	7	8	9	>=9.5	No comp.	6.DP

Figure 1 Pairwise comparison judgement.

Table 1 Nine-point scale judgement [8].

Numerical value	Preference level
1	Equally preferred
2	Equally to moderately preferred
3	Moderately preferred
4	Moderately to strongly preferred
5	Strongly preferred
6	Strongly to very strongly preferred
7	Very strongly preferred
8	Very strongly to extremely preferred
9	Extremely preferred

3. RESULTS AND DISCUSSION

The results of the AHP method to prioritize the PDS criteria shown in table 2 and figure 2. It shows that the highest rank of decision makers choice went to performance (PF) with average value of 0.359 which means 35.9% from overall PDS criteria. Seven out of ten decision makers chose performance (PF) as the important criteria to be the side-door impact beam while six give the size (SZ) as the least criteria to be look at. Product cost (PC) in second rank with value of 0.194, followed by weight (WG) with value of 0.173, environment (EV) and disposal (DP) in fourth and fifth rank with value of 0.112 and 0.085, respectively and finally size (SZ) falls in the last rank with value of 0.077.

Table 2 Prioritize PDS criteria for side-door impact beam.

	PF	SZ	WG	PC	EV	DP
DM1	0.577	0.073	0.071	0.134	0.073	0.073
DM2	0.556	0.110	0.110	0.142	0.041	0.041
DM3	0.349	0.060	0.031	0.349	0.153	0.059
DM4	0.313	0.034	0.044	0.339	0.104	0.166
DM5	0.525	0.023	0.185	0.075	0.097	0.097
DM6	0.385	0.044	0.385	0.093	0.046	0.046
DM7	0.292	0.292	0.031	0.292	0.046	0.046
DM8	0.235	0.059	0.235	0.235	0.118	0.118
DM9	0.179	0.031	0.556	0.172	0.031	0.031
DM10	0.181	0.046	0.078	0.110	0.414	0.170
Σ	3.592	0.772	1.726	1.941	1.123	0.846
AVE	0.359	0.077	0.173	0.194	0.112	0.085

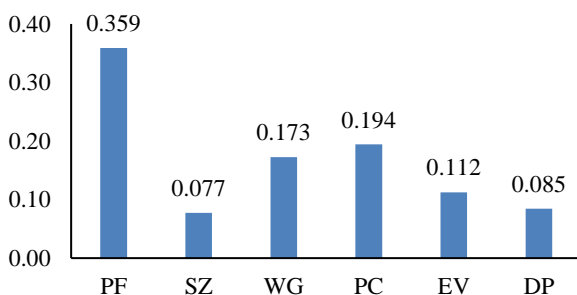


Figure 2 Prioritize value for PDS criteria of side-door impact beam.

4. CONCLUSIONS

In conclusion, prioritizing PDS criteria for side-door impact beam can be made using AHP method. In this study, the pairwise comparison judgement were made by ten decision makers and analysed using Super Decisions software.

The results then were recorded for each PDS from each decision makers. From the judgement, performance (PF) is the highest priority set by the average marks of decision makers followed by product cost (PC), weight (WG), environment (EV), disposal (DP) and size (SZ). For future works, the priority criteria shall be used for conceptual design development and selection in the next product development process.

ACKNOWLEDGEMENT

The authors would like to thank Universiti Putra Malaysia for the financial support provided through the Putra Grant IPS (GP-IPS/2016/9515100), as well as Universiti Teknikal Malaysia Melaka and Ministry of Higher Education Malaysia for providing scholarship to the principal author to carry out this research project.

REFERENCES

- [1] Hedeon, C. E., Campbell, D. D. (1969). Side impact structures. 1969 International Automotive Engineering Congress and Exposition, SAE 690003.
- [2] Cerniauskas, E., Kersys, A., Lukosevicius, V., & Sapragonas, J. (2010). Impact of anti-intrusion beam effectiveness on reducing fatalities and injuries of vehicle occupants. *Mechanika*, 86, 11-16.
- [3] Teng, T. L., Chang, K. C., & Nguyen, T. H. (2008). Crashworthiness evaluation of side-door beam of vehicle. *Technische Mechanik*, 28(3-4), 268-278.
- [4] Pugh, S. (1993). Total Design: Integrated Methods for Successful Product Engineering, Addison.
- [5] Mansor, M. R., Sapuan, S. M., Zainudin, E. S., Nuraini, A. A., & Hambali, A. (2013). Hybrid natural and glass fibers reinforced polymer composites material selection using Analytical Hierarchy Process for automotive brake lever design. *Materials & Design*, 51, 484-492.
- [6] Mastura, M. T., Sapuan, S. M., Mansor, M. R., & Nuraini, A. A. (2017). Conceptual design of a natural fibre-reinforced composite automotive anti-roll bar using a hybrid approach. *The International Journal of Advanced Manufacturing Technology*, 91(5-8), 2031-2048.
- [7] Saaty, T. L. (1990). How to make a decision: the analytic hierarchy process. *European journal of operational research*, 48(1), 9-26.

Mastura, M. T., Sapuan, S. M., Mansor, M. R., & Nuraini, A. A. (2017). Environmentally conscious hybrid bio-composite material selection for automotive anti-roll bar. *The International Journal of Advanced Manufacturing Technology*, 89(5-8), 2203-2219.

The formation of tribo-chemical protective layer of bio-lubricant during friction test

Nor Azmmi Bin Masripan^{1,2,*}, Husna A. Hamid^{1,2}, Mohd Fadzli Bin Abdollah^{1,2}, Ghazali Omar^{1,2},
Imran Syakir Mohamad^{1,2}, Nurfaizey Abdul Hamid^{1,2}

¹⁾ Faculty of Mechanical Engineering, Universiti Teknikal Malaysia Melaka,
Hang Tuah Jaya, 76100 Durian Tunggal, Melaka, Malaysia

²⁾ Centre for Advanced Research on Energy, Universiti Teknikal Malaysia Melaka,
Hang Tuah Jaya, 76100 Durian Tunggal, Melaka, Malaysia

*Corresponding e-mail: norazmmi@utem.edu.my

Keywords: Protective layer; bio-lubricant; friction

ABSTRACT – The aimed of this study is to investigate the formation of tribo-chemical protective layer of bio-lubricant from banana peel waste during friction test. The bio-lubricant is extracted from banana peel waste of Musa Aluminata Balbisiana (MBS). Tribological evaluation of MBS oil was conducted using pin-on-disc tribometer as per ASTM G 99 standard. In this study, bio-oil was used as a lubricating oil on sliding surface at varying loads and temperature. It was obobservinggthrough microscopic analysis that, the formation of tribo-chemical film which existed as protective layer on sliding surface thus preventing the contact between two surfaces.

1. INTRODUCTION

Banana skin has been often referred as slipping tools by the literature [1-3]. Previous study had showed that coefficient of frictions under epicarp of banana skin; on the floor material is much lower to the value of common materials and similar to the well-lubricated surface. Lubricating effect of banana skin is contributed by the existence of follicular gel, which is sized about a few micrometers [1]. Another study found that, percentages of extraction yields of bio oil from the peel waste of banana species were influenced by the existence of follicular gel [4]. The follicular gel was analyses using scanning electron microscopes and they concluded that, the polysaccharide follicular gel is a major key element in formation of oil [4,5]. Hamid et al., [2] investigated the effects of banana peel of Cavendish species as a natural additive in paraffin oil. The tribological properties of the specimens were evaluated using four-ball tester. The coefficient of friction, COF and wear significantly reduced at high load, temperature and speed.

The mechanism that affect the tribological performance of bio-lubricant is still limited. Hence, the objective of this paper is to to investigate the formation of tribo-chemical protective layer of bio-lubricant from banana peel waste during friction test.

2. METHODOLOGY

In this study, the tribological testing was performed according to the ASTM G99-05 standard under lubricated sliding conditions at different temperatures and applied load. A constant sliding speed and wear track diameter were applied along the

experiments as shown in Table 1. The pin was heated using an external heat resource where a thermocouple was placed on the edge of the counterpart pin. Time was set according to the time of test that would be conducted. An infrared thermometer (Extech 42580) was used to measure the temperature. It was pointed at the specimen before the test began. Morphological characterization of the pin surface was carried out using Scanning Electron Microscopy (SEM). The electrons in the beam interact with the sample producing various signals that can be used to obtain information about the surface topography and composition (EDX). The surfaces of all the samples were coated with a thin film of platinum using Polaron SC 7640 Sputter in order to improve the conductivity and avoid electron-charging effects during analysis.

Table 1 Pin-on-disc test parameters.

Test Parameter	Value
Loads (N)	20, 40, 60, 80, 100
Temperatures (°C)	27, 40, 100
Sliding speed (RPM)	50
Sliding distances (m)	314
Sliding Times (minutes)	50

3. RESULTS AND DISCUSSION

A tribo-chemical reaction may occur between fatty acids composition in MBS oil with the disc surface, which may have resulted in the formation of metallic soap layer, and fluid protective layer that contributed to the favor of frictional reduction as shown in Figure 1. Pin was believed to exist as contacting surface while disc acts as opposing contacting surface. The higher magnitudes of COF at the beginning of sliding indicates that the lubrication regime occurred in the rubbing zone is boundary lubrication. Moreover, at this phase, the fluid protective film was fully developed with functioned to protect the contacted surface. At all the tested temperatures of the load of 80 N, it shows the greatest ability to retain its properties without the breakdown of the lubrication film. In this study, at higher load (80 N), the lubricating film thickness become thinner than some of the asperities present in the boundary lubrication. However, the asperities are covered by the long chain fatty acids and the ester of biolubricants, which are known as surface-active materials.

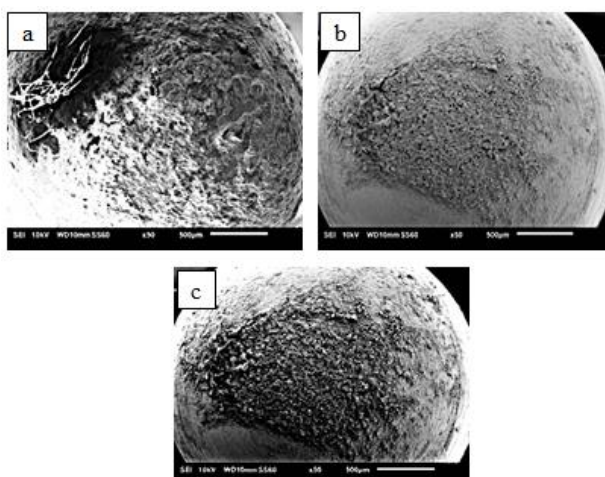


Figure 1 SEM micrograph of monolayer of tribo-chemical film at the hemisphere surface of the pins at (a) 27 °C, (b) 40 °C and (c) 100 °C.

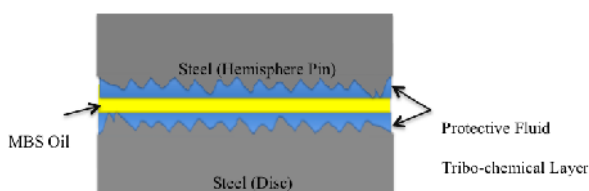


Figure 2 A schematic representation of tribo-chemical's film and its corresponding contact mechanism in pin on disc under lubrication of MBS oil.

The presence of adsorption of polar molecules such as long chain fatty acids and ester in bio-lubricants act as an efficient barrier for protective sliding surface contact and friction surface and lead to the reduction in COF. In addition, the existences polar group of esters also provides an affinity to metal surface and contributed to the formation of protective layer between metal surfaces. In other words, the polarity of the ester group creates a strong affinity to the metal by one end of the molecules and it's allowed a nonpolar hydrocarbon to extend out and provides a barrier between surfaces. Moreover, the presence of carbonyl group in MBS oil was believed to be chemically and physically adsorbed onto the steel or metal surface. The adsorption therefore provides a prevention of direct contact between frictional pairs due to the formation of orderly and closely packed molecular multi layers. A schematic representation of chemical adsorption of fatty acids

molecules of MBS oil on surfaces during friction. Furthermore, fatty acids molecules which known as corrosive component, was believed can cause the corrosion and material removal of fractional pairs.

4. CONCLUSION

The investigation on tribological properties of MBS oil was successfully performed using pin on disc tribometer. The formation of tribo-chemical film was observed at the contact surface which acting as protective-layer during friction. The finding from this study might contribute to the sustainable development of the bio-lubricants fields.

ACKNOWLEDGEMENT

The authors would like to acknowledge the Faculty of Mechanical Engineering, Universiti Teknikal Malaysia Melaka for financial support through research grant FRGS/1/2016/TK10/UTEM/02/F00275 and the Ministry of Higher Educations (MOHE), which made this study possible.

REFERENCES

- [1] Mabuchi, K., Tanaka, K., Uchijima, D., & Sakai, R. (2012). Frictional coefficient under banana skin. *Tribology Online*, 7(3), 147-151.
- [2] Hamid, A. H., Masripan, N. A. B., Basiron, J., Mustafa, M. M. B., Hasan, R., Abdollah, M. F. B., & Ismail, R. (2015). Effect of banana peels as an additive on the tribological properties of paraffin oil. *Jurnal Teknologi (Science and Engineering)*, 77(21), 73-77.
- [3] Azmi, M. I. R., Tee, B. T., Masripan, N. A. B., & Chong, C. T. (2015). Preliminary study of friction and wear on natural oil-based lubricants. *Proceedings of Malaysian International Tribology Conference, 2015*, 220-221.
- [4] Hamid, H. A., Masripan, N. A. B., Hasan, R., Abdollah, M. F. B., & Omar, G. (2016). Characterization of raw and ripen banana peel wastes and its oil extraction using soxhlet extraction method. *International Journal of Applied Chemistry*, 12(1), 1-5.
- [5] Foidl, N., & Eder, P. (1997). Agroindustrial Exploitation of *Jatropha curcus*. *Bio-fuels and Industrial Products from Jatropha Curcas*. Graz: Dbv-Verlag, 88-91.

Development Of volatile organic compounds (VOC) removal filter for transport air-conditioner and VOC removal test

Norain Idris^{1,*}, Syazwan Sukri², Intan Mastura Saadon³

¹⁾ Faculty of Engineering Technology, Universiti Teknikal Malaysia Melaka, Hang Tuah Jaya, 76100 Durian Tunggal, Melaka, Malaysia.

²⁾ Centre for Advanced Research on Energy, Universiti Teknikal Malaysia Melaka, Hang Tuah Jaya, 76100 Durian Tunggal, Melaka, Malaysia.

*Corresponding e-mail: norain.idris@utem.edu.my

Keywords: VOC filter; odour filter; transport air-conditioner

ABSTRACT – Bad odour creates an uncomfortable atmosphere to driver and passengers. Therefore, an odour removal filter with activated carbon as an absorbent agent is developed for an existing car air-conditioner system, particularly for 1.3cc Perodua Myvi car. Since bad odour is linearly correlated with VOC concentration, VOC level reduction is measured before and over 60-minute-after the filter installation by using 3M EVM Environmental Monitor Kit. The VOC filter prototype is tested by using two VOC sources; that are cigarette smoke and oil paint. Results show that the VOC filter is capable to remove the VOC level up to 15%.

1. INTRODUCTION

Air conditioning system create a comfortable cool air for environment by controlling the temperature of the air, humidity and indoor air quality [1]. In any air-conditioning system inclusive in transportation, air filter is utilized to avoid the driver and passengers from being exposed to diseases in polluted air by filtering out dust and contaminant [2]. However, the existing transportation air-conditioning air filter is unable to remove bad odour. Among the causes is cigarette smoke. Smoking inside small enclosed space such as a car particularly dangerous because smoke can accumulated rapidly as stated in previous study [3], if the smoke is not removed. Henceforth, an odour removal filter is developed to counter the bad odour specifically in a 1.3cc Perodua Myvi car cabin. Since bad odour is caused by certain Volatile Organic Compounds (VOC) substances and linearly correlated with VOC concentration [4], the filter is tested by measuring the decrease of VOC level before and after the VOC filter installation.

2. METHODOLOGY

2.1 Product design

The VOC removal filter is designed by using AutoCad software by taking several criteria into account. They are VOC absorption efficiency, filter life expectancy, undisturbed air flow, low cost and filter weight. Following Figure 1 shows the developed 1.3cc Perodua Myvi VOC filter size, whereby the filter width x length x thickness is 160 mm (W) x 160 mm (L) x 3 mm (T). According to the design, a prototype is developed with activated carbon as filter agent.

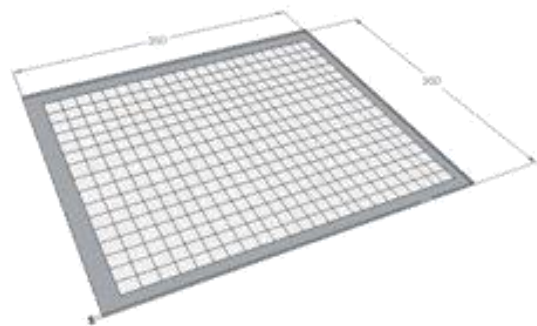


Figure 1 Designed VOC filter for Perodua Myvi.

2.2 Data collection

VOC filter is installed in 1.3cc Perodua Myvi car, sandwiched with the existing air conditioner filter. The VOC filter data performance is observed by using 3M EVM Environmental Monitor Kit which uses photoionization detector (PID), with display resolution between 0.01 and 1 in ppb (equivalent to mg/m³) unit. It has +5% of accuracy and 2% repeatability at calibration level.

The data are collected before the car air conditioner is started and during every 10-minute operation for 60 minutes. The sample of VOC source such as oil paint and cigarette smoke are introduced inside the car cabin. The VOC filter performance efficiency is then analyzed by using precendently measured in-operation VOC level series without VOC filter as baseline.

3. RESULTS AND DISCUSSION

The results of the findings are presented by line graphs to show gradual reduction of VOC level in parts per million (ppm) over time. For every VOC source, VOC ppm data comparison between with and without VOC filter can be extracted from the graphs. The data collection is done in a closed area, that is inside the car cabin, with all possible air intrusion locations such as doors and windows closed. The data are taken at two locations, that are in the middle of the front and back passenger seat. The VOC level measurement of both locations are accumulated, and the average data is herewith calculated.

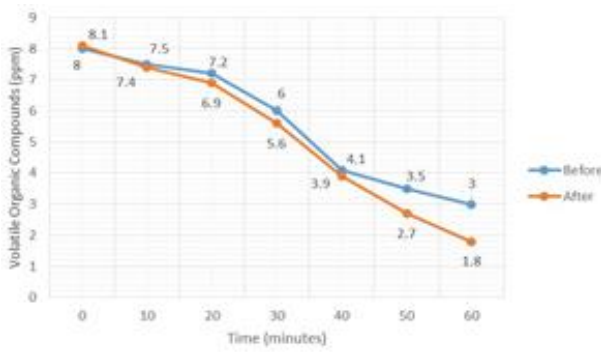


Figure 2 VOC at ppm level over time for cigarette smoke.

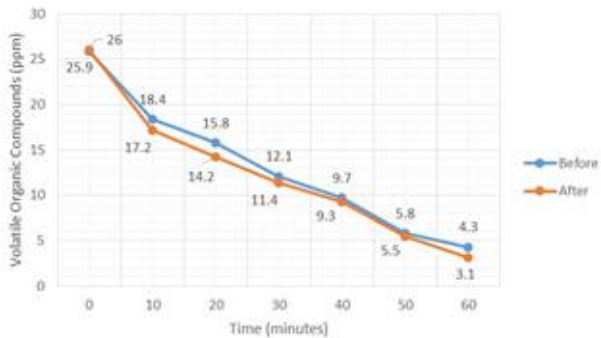


Figure 3 VOC at ppm level over time for oil paint.

Based on the data in Figure 2, the total reduced percentage of VOC in the cabin air for cigarette smoke without the VOC filter installation is 62.5%. Meanwhile, the total percentage of VOC reduction is 77.77%. This indicates that the VOC filter is capable to remove further 15.27% of VOC level if compared to the existing air-conditioner air filter system.

In Figure 3, it can be extracted that the total reduced percentage of VOC level in the cabin air with oil paint as VOC source is 83.4% without VOC filter installation. With VOC filter in action, VOC level is reduced more to 87.74%. In other words, the VOC filter manages to filter 4.34% better compared to that without the VOC filter.

The results show that activated carbon is capable to remove VOCs at ppm level and this is in good agreement with previous study by [5]. The difference of the total reduced percentage of VOC level for different VOC source is most probably due to various existed chemical substances and concentration in every source. Moreover, most probably the filter agent, that is activated carbon could only filter out certain chemical substance and concentration up to certain level. This observation is evident according to previous study [4].

The VOC level readings in ppm are taken by taking pictures from outside of the windows to prevent air

intrusion via door and to avoid the accumulated VOC inside the cabin from escaping. This will lead to higher uncertainty and inaccurate results. In addition, the measurement device is extremely sensitive and any exposure to even slow wind could affect the readings. Thus it is best to avoid close contact with the device.

4. CONCLUSIONS

The VOC filter prototype design is developed with aid of AutoCad software and the size is customized to 1.3cc Perodua Myvi car air-conditioner. Activated carbon has been selected as VOC absorbent based on certain criteria in concept scoring stage. Apart from that, the prototype of VOC filter is installed after the existing filter to avoid disturbance of the air-conditioner system's original function. The aim of the filter is only to reduce VOC level from the existing filtered air.

Series of every-ten-minute VOC ppm shows that activated carbon can be used to remove certain level of VOC. Evident reduction of VOC level is showed by two different VOC sources, that are cigarette smoke and oil paint. This result is in good agreement with previous study by [5], which stated that activated carbon is a potential adsorbent for capturing VOCs at ppm levels. This ranges from 4% to 15%. The different VOC reduction showcase in both sources is most probably due to different chemical reaction of activated carbon to distinct chemical substances in the VOC sources.

REFERENCES

- [1] Oh, M. S., Ahn, J. H., Kim, D. W., Jang, D. S., & Kim, Y. (2014). Thermal comfort and energy saving in a vehicle compartment using a localized air-conditioning system. *Applied Energy*, 133, 14-21.
- [2] Boni, A., & Clark, M. (2008). Filter media: Improving filter media to achieve cleaner air. *Filtration & Separation*, 45(9), 20-23.
- [3] Murphy-Hoefer, R., Madden, P., Maines, D., & Coles, C. (2014). Prevalence of smoke-free car and home rules in maine before and after passage of a smoke-free vehicle law, 2007–2010. *Preventing Chronic Disease*, 11.
- [4] Noguchi, M., Tanaka, S., Watanabe, K., & Yamasaki, A. (2016). Correlation between odor concentration and volatile organic compounds (VOC) composition of environmental tobacco smoke (ETS). *International Journal of Environmental Research and Public Health*, 13(10), 1-12.
- [5] Das, D., Gaur, V., & Verma, N. (2004). Removal of volatile organic compound by activated carbon fiber. *Carbon*, 42(14), 2949-2962.

Improvement of engine performance of a single-cylinder compression ignition engine using 3d-printed helical thread intake manifold

A.A. Hairuddin*, M.A. Shafanejad

Department of Mechanical and Manufacturing Engineering, Faculty of Engineering, Universiti Putra Malaysia, 43400 UPM Serdang, Selangor, Malaysia.

*Corresponding e-mail: ahziz@upm.edu.my

Keywords: Intake manifold; helical threaded; diesel engine

ABSTRACT – Over past decades different types of intake manifolds had been introduced but there are limited literatures about the behavior of helical threaded intake manifold with a clear classification. This study emphasis of the comparison for performance of a single cylinder engine with three different intake manifolds. The manifolds (trapezoidal and circular) have been printed by using 3D-printer to the engine parameters such as torque, emission level, power output and specific fuel consumption. The highest value of torque is 11.6 Nm at 1500 rpm which belongs to circular threaded intake manifold. The NO_x emission level for trapezoid threaded intake manifold in overall is lower than other two intake manifolds. The CO emission level for circular threaded intake manifold is slightly higher than the trapezoidal threaded intake manifold meanwhile the current intake manifold has the highest CO emission level. The highest power output belongs to circular threaded intake manifold at 3030 W. Circular threaded intake manifolds is good to be investigated for future studies.

1. INTRODUCTION

The number of vehicles on the road are keep increasing which causes the high level of pollution. Caustically, the major challenge in automotive industries are the design of the engine, which has low engine efficiency and an inefficient volumetric air flow. There exist raise in demand for maximum fuel saving and thermal efficiency by consumers and for better quality in small capacity engines [1]. To address this issue, several researches have been conducted in the past and are still ongoing which include the new designs and optimization of existing intake manifold system [2-3]. Optimizing the existing design of the intake manifold to deduct overall pressure drop across air intake system plays a vital role in developing engine performance characteristic in terms of power, fuel economy and emission [3-5]. Therefore, this study focuses to investigate the effect of two different threaded air intake manifolds on the engine performance.

2. METHODOLOGY

The models were 3d printed to produce the prototype for experimental investigations. The 3D printer model is Ultimaker which has the ability to print the product of 12x12x12 cm in size. The material is Polylactic Acid (PLA) plastic. Both air intake models are as shown in Figure 1 and 2. Once the prototyping has been completed, the new intake manifold was installed on a single cylinder diesel engine (Yanmar L48AE), with capacity of 211 cc. The engine was connected to an eddy

current dynamometer. The emissions levels were measured using EMS 5002 gas analyser. The experiment was conducted from 1500 – 3000 rpm. Figure 3 shows the engine setup and how the intake manifold installed on the engine.

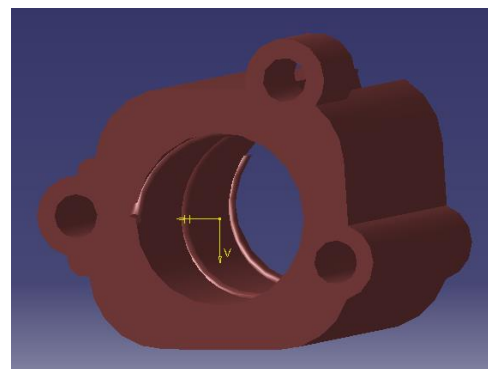


Figure 1 Circular threaded air intake manifold.

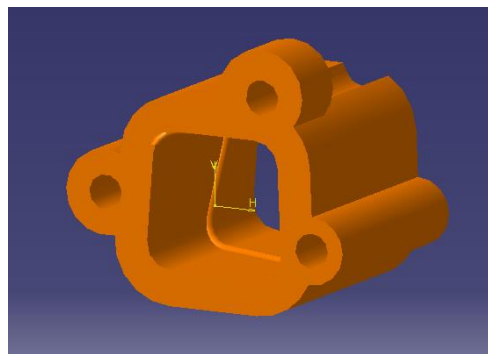


Figure 2 Trapezoidal threaded air intake manifold.



Figure 3 Engine setup and the location of the intake manifold.

3. RESULTS AND DISCUSSION

3.1 Engine power

Figure 4 shows that engine speed is varied from 1500 to 3000 RPM with the step size of 100 RPM for three of the intake manifolds, circular, trapezoidal and current intake manifolds. The highest power output belongs to circular threaded intake manifold which the value of it is 3030 W at 2500 RPM. Meanwhile the value of power output for trapezoid threaded intake manifold and current intake manifold at the same engine speed are 3000.2 W and 2996.6 W. The engine torque, also shows that, the circular threaded intake manifold has the highest value of 11.6 Nm at 1500 RPM. This result indicates that the circular threaded intake manifold produces a better air flow with improved swirl. The swirl will then affect the mixing of fuel and air in the combustion chamber and hence, improved the mixing rate and yields better combustion.

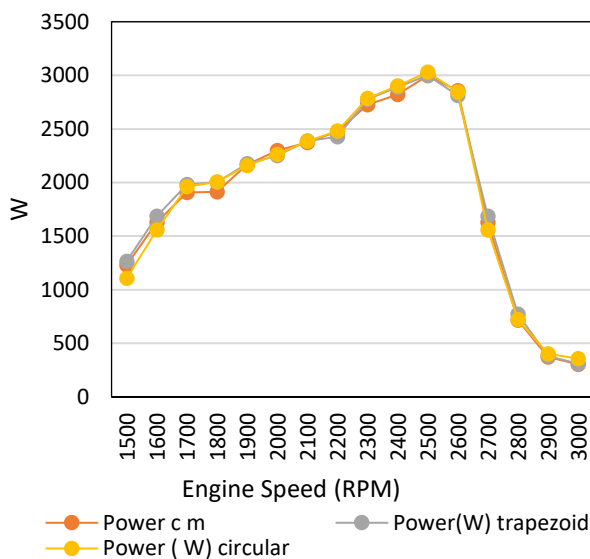


Figure 4 Engine torque comparison for three different intake manifolds: current, circular and trapezoidal.

3.2 Emissions Levels

Figure 5 shows the CO emissions from 1600 to 3000 rpm. It shows that for trapezoidal and circular threaded intake manifolds, the emission level of CO is quite similar to each other but for circular threaded intake manifold is slightly higher from trapezoid threaded intake manifold until 2000 rpm. Meanwhile the current intake manifold has the highest emission level among all three intake manifolds. As for CO₂, the current intake manifold produced the highest emission between 1800 and 2200 RPM. NO_x emission level, on the other hand, shows that the circular threaded intake manifold is higher than other intake manifolds between 2000 and 2800 RPM. The NO_x emission level for trapezoidal threaded intake manifold in overall is lower than other two intake manifolds.

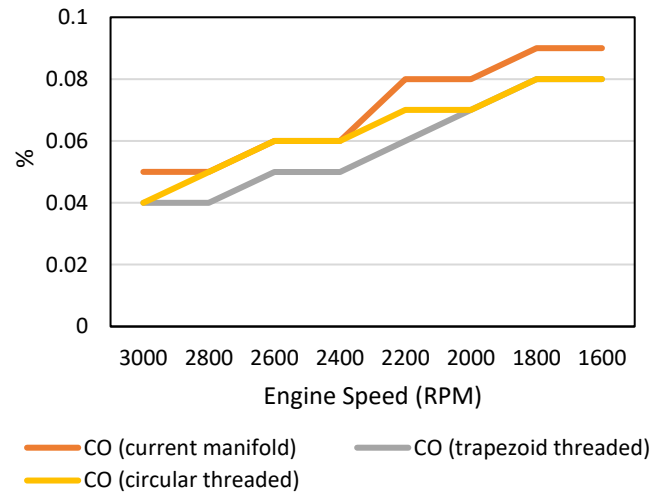


Figure 5 CO comparison for three different intake manifolds.

4. CONCLUSION

In conclusion, the highest power output belongs to circular threaded intake manifold which has the value of it is 3030 W at 2500 RPM, about 1% improvement in engine power. The torque, on the other hand, shows about 0.8% improvement over the current intake manifold. The results of emissions levels are varied among the intake manifold; however, circular threaded intake manifold has the potential to be improved for future studies.

ACKNOWLEDGEMENT

This project is supported by Universiti Putra Malaysia (grant number: GP-IPM/2016/9483100).

REFERENCES

- [1] Sonawane, P., & Patil, P. (2016). Design and development of swirl chamber type induction system for a four stroke petrol engine - A review. *International Conference on Global Trends in Engineering, Technology and Management*, 234-237.
- [2] Heywood, J. (1988). *Internal Combustion Engine Fundamentals*.
- [3] Mohamed, M. A. (2010). *Intake and Exhaust Ports Flow Investigation of 4-stroke SI Engine* (Thesis, UMP).
- [4] Bell, A. G. (1998). *Four-stroke Performance Tuning*. Cambridge University Press.
- [5] Ceviz, M. A., & Akın, M. (2010). Design of a new SI engine intake manifold with variable length plenum. *Energy Conversion and Management*, 51(11), 2239-2244.